Development and Testing of a Passive Variable-Pitch Propeller

Stearns B. Heinzen,* Charles E. Hall, Jr.,† and Ashok Gopalarathnam†
North Carolina State University, Raleigh, North Carolina 27695

DOI: 10.2514/1.C032595

A novel approach to passive propeller blade pitch variation is investigated. To effect passive pitch changes, the propeller blades are allowed to pivot freely about a radial axis, and aerodynamic pitching moments are tailored to give favorable blade pitch angles over a wide range of advance ratios. Computational modeling of the system indicated that a large expansion of the efficient operating envelope is possible, compared to a fixed-pitch propeller. Wind-tunnel experiments corroborated the computational results and demonstrated that the propeller maintained near-peak efficiency by passively adjusting blade pitch angles by over 15 deg to the match changing advance ratio. The passive variable-pitch propeller was then successfully demonstrated in flight on an unmanned aerial vehicle. Using tailored aerodynamics in place of active control allows this performance improvement to be realized at a fraction of the weight and complexity of a traditionally actuated variable-pitch propeller. The concept enables the benefits to be realized on platforms for which a traditional constant-speed variable-pitch propeller is not viable, such as on small general aviation aircraft or on unmanned platforms.

Nomenclature

$\boldsymbol{BCG}$	=	position vector from BLADE-frame origin to blade center of gravity
C_L	=	total blade lift coefficient
C_M	=	total blade pitching-moment coefficient
C_P	=	propeller power coefficient; $P/\rho n^3 D^5$
C_T	=	propeller thrust coefficient; $T/\rho n^2 D^4$
C_d	=	local drag coefficient
C_l	=	local lift coefficient
C_{lo}	=	zero-α lift coefficient
$C_{l\alpha}$	=	lift-curve slope
C_m	=	local pitching-moment coefficient about the moment reference center
c	=	$c(r)$; chord as a function of radial location
$\bar{c}'$	=	weighted mean aerodynamic chord
D	=	propeller diameter
F_D	=	aerodynamic drag force parallel to local flow direction
F_Q	=	blade-element force in plane of propeller rotation
$\boldsymbol{H}$	=	blade angular momentum vector
$\boldsymbol{I}$	=	inertia tensor for single propeller blade
$\boldsymbol{ICG}$	=	position vector from INERTIAL-frame origin to blade center of gravity
J	=	advance ratio; V/nD
L	=	lift oriented perpendicular to local flow direction
M	=	pitching moment about blade pitch axis
m	=	entire mass of a single blade with balancing masses
n	=	propeller rotations per second
P	=	shaft power absorbed by propeller
Q	=	torque per blade
q	=	dynamic pressure
r	=	local radial position
R	=	propeller radius
S'	=	weighted planform area for blade
SM'	=	weighted static margin for blade
T	=	propeller thrust per blade
V	=	flow velocity
w	=	weighting factor for radial velocity variation; $[1 + (\pi r/JR)^2]$
X'_{ac}	=	overall weighted blade aerodynamic center
x_{ac}	=	chordwise distance between blade-pivot axis and local-section aerodynamic center
α	=	local angle of attack
β	=	$\beta(r)$; base blade twist relative to the propeller plane of rotation
$\Delta\beta$	=	change in propeller blade pitch angle from baseline
η	=	propeller operating efficiency
ρ	=	atmospheric density
Ω	=	propeller rotational speed
$\boldsymbol{\omega}$	=	propeller angular velocity vector

Subscripts

ac	=	about aerodynamic center
l	=	local conditions for a blade element
r	=	rotational component
∞	=	freestream

I. Introduction

THE process of matching a fixed-pitch propeller to a given engine/airframe combination is an exercise in compromise. A pilot desiring climb performance will reduce the propeller pitch, improving efficiencies at low propeller advance ratios at a cost to high-speed performance. Conversely, tailoring for cruise performance will negatively impact field performance. Although the earliest propellers were of the fixed-pitch configuration, the potential benefit of a variable-pitch propeller was realized conceptually, if not in practice, in the late 1800s [1]. Variable-pitch propellers implemented in the 1930s yielded improvements to short-field performance, maximum flight speeds, and altitudes [2,3]. They are used on most modern high-performance reciprocating and turboshaft aircraft, allowing the propeller to produce efficient thrust over the entire flight envelope. For those aircraft too small to support the weight and complexity of a variable-pitch propeller, such as ultralight aircraft and many unmanned systems, and for aircraft that are not allowed the use of a variable-pitch propeller, such as light sport aircraft, performance compromises must be accepted.

The past decade has witnessed unprecedented growth in the unmanned air vehicle (UAV) flight hours flown by the military [4], and the next decade will see a similar pattern in the civilian realm. Many of the current small UAVs fall in a category where navigation, control, and many avionics systems have become increasingly sophisticated. In contrast, propulsion systems often lag, largely using

Presented as Paper 2012-1068 at the 50th Aerospace Sciences Meeting, Nashville, TN, 9–12 January 2012; received 28 August 2013; revision received 27 February 2015; accepted for publication 13 March 2015; published online 24 April 2015.

*Teaching Assistant Professor, Mechanical and Aerospace Engineering; currently Aerospace Engineer, Naval Research Laboratory, Washington, D.C. 20375; stearns.heinzen@nrl.navy.mil. Senior Member AIAA.

†Associate Professor, Mechanical and Aerospace Engineering, Campus Box 7910. Associate Fellow AIAA.

retrofitted radio-control and ultralight equipment. Consequently, new high-performance airframes often rely on relatively primitive propulsive technology. This trend is beginning to shift with recent advances in small turboshaft engines, fuel-injected reciprocating engines, and improved electric technologies. Although these systems are technologically advanced, they are often paired with standard fixed-pitch propellers. To fully realize the potential of these aircraft and the new generation of engines, propellers that can efficiently transmit power over wide flight envelopes and a variety of power settings must be developed.

For any aircraft, the potential performance benefit of a propeller that adjusts to changing advance ratio depends largely on the type of mission the vehicle in question will fly. The wider the typical flight envelope, the greater the potential benefit from such a propeller. An extreme is represented by a future mission for a large bird-sized propeller-driven UAV. Mission phases could include low-speed or hovering launch, rapid transit to a location of interest where the UAV could circle slowly to surveil, or a perch on an available surface or power line. In the course of tracking an object or person, the UAV may repeat several cycles of hovering takeoff to transit to perch landing before terminating the mission with a rapid transit [5]. This type of mission would include propulsive requirements from a high-thrust zero-airspeed condition, required during hovering takeoff and perch landings, to rapid transit dashes at significantly higher advance ratios. Accomplishing the mission effectively requires a vehicle capable of producing efficient thrust during all mission phases.

Variable-pitch propellers are typically actuated hydraulically or, less frequently, electrically. Systems of this type, although appropriate for many general aviation aircraft, present excessive weight and complexity for use on most small unmanned vehicles. Several propeller concepts attempt to address the weight and complexity issue using a variety of aerodynamic, aeroelastic, mass-balancing, and/or spring-driven approaches[§] [6–9]. Some of these designs are found on flying aircraft today, whereas others have been tested only in the laboratory setting. For any system to be viable, whatever mechanism it uses, it must be very light, and it must have a low part count and integration cost.

This paper discusses a proposed system comprising a propeller designed to passively adjust to the incoming airflow to prevent blade stall in low-velocity/high-thrust conditions and overspeeding at high flight speeds. As illustrated in Fig. 1, the propeller incorporates blades that rotate freely in pitch on a radial pivot axis and are aerodynamically tailored to attain and maintain a pitch angle yielding favorable local blade angles of attack, matched to the changing advance ratio. This blade pitch angle is achieved through the use of reflexed airfoils designed for positive pitching moments comparable to those used on many tailless flying wings. By setting the axis of pitch rotation at a point forward of the blade aerodynamic center, the blades naturally adjust to a predetermined positive-lift "trim" condition. Then, as the advance ratio changes, the blade pitch angle adjusts to maintain the same angle with respect to incoming air. Because the system uses only the aerodynamic loads on the rigid blades for pitch control, parts in the hub are limited to passive mass balancing and a simple gear linkage to ensure symmetric blade pitch angles.

This approach to pitch variation is unique among other current passive techniques because of the manner in which the moment balancing parameters vary with operating condition. The earliest passive varying-pitch propeller is the "Aeromatic" propeller designed for small general aviation aircraft in the 1930s. This propeller balances moments generated by propeller aerodynamic forces with inertial moments generated by an off-pivot-axis blade center of gravity[§] [6]. A second approach [7] uses a motor shaft torque to compress a torsional spring in the hub, where the torsional spring acts on blade pitch with the intent of keeping torque constant. Other approaches have employed aeroelastic tailoring for in-flight variation of blade twist from aerodynamic loads or a combination of aerodynamic and inertial loading [8,9]. In all of these cases, balanced

[§]Aeromatic Air Controlled Automatic Propeller Website, Data available online at http://www.aeromatic.com [cited 27 March 2015].

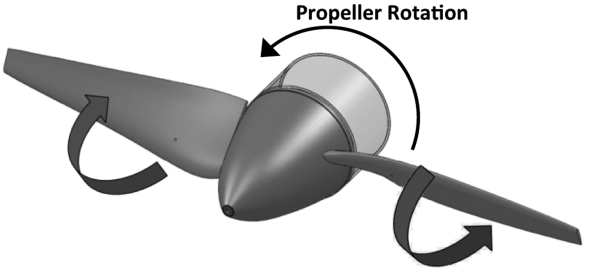

Fig. 1 Illustration of a passive variable-pitch propeller. Wide arrows indicate positive blade pitch (i.e., larger $\Delta\beta$).

pitching moments include at least one nonaerodynamic component: inertial forces and moments, structural stiffness, or a spring system. This nonaerodynamic component results in a nonunique blade pitch angle for a given advance ratio. The current approach uses purely aerodynamic moments: one generated by the pitching moment about the blade aerodynamic center, and the other by the lift acting at the aerodynamic center generating a moment about the blade-pivot axis. Both of these moments scale in the same proportion with changing atmospheric conditions and with changing dynamic pressure, and so yield a unique blade equilibrium angle for a given advance ratio.

The governing equations for a simplified model of a passive variable-pitch propeller (PVPP) are presented. The main intent is to have available approximate closed-form equations and relationships that are helpful in determining the main design parameters, and are suitable for use in the early design phases of a PVPP. The main approximation in this model is that induced inflow is neglected; the errors from this approximation tend to become more significant at low advance ratios. Computational methods for aerodynamic analysis are then presented. In contrast to the approximate model, the computational approach takes into account the induced-inflow velocities, and is therefore appropriate for the lower advance ratios. The disadvantage of the computational methods, however, is that they do not present relationships in closed form, and the effects of various parameters must be determined by parametric studies. The development of candidate test propellers is described, followed by experimental results from wind-tunnel and flight tests, demonstrating the effectiveness of the PVPP concept.

II. Development of the Governing Equations for an Approximate Model

A. Characterization of Propeller Thrust and Torque

Propeller coefficients are typically nondimensionalized and plotted versus the propeller advance ratio J, which is proportional to the ratio of the freestream flow velocity to the blade rotational velocities:

$$J = \frac{V_\infty}{nD} \tag{1}$$

A given J defines the inflow angle at any point of the blade and, for a propeller blade at a static pitch angle, the angle-of-attack distribution. When plotting propeller coefficients, the advance ratio is the natural choice of independent variable, as it maps to the general angle-of-attack state of the propeller blade over the operating range. The typical propeller coefficients most relevant to analyzing propeller performance are the thrust and power coefficients, relating the output and input of the propeller, i.e.,

$$C_T = T/\rho n^2 D^4 \tag{2}$$

and

$$C_P = P/\rho n^3 D^5 \tag{3}$$

Combining them with the advance ratio yields the overall efficiency of the propeller,

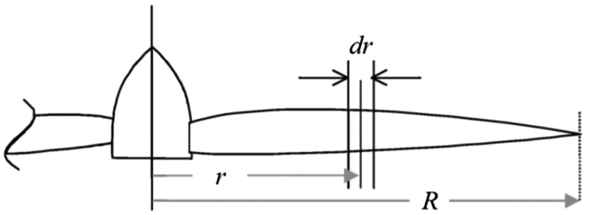

Fig. 2 Blade element at radial location *r*.

$$\eta = TV_\infty/P = C_T J/C_P \tag{4}$$

These coefficients can be determined from measured propeller thrust, torque, rotational speed, and freestream velocity. Early in development, however, the cost of experimental analysis is prohibitive in both time and material, and an analytical/ numerical approach is preferred. The common initial approach combines an actuator-disk flow model with a blade-element propeller model. Figure 2 shows a typical element of the propeller blade.

In this approximate model, induced flow is assumed to be small compared to V_∞, so as to develop closed-form relations. With this assumption, as shown in Fig. 3, the local velocity V_l at any radial location r depends on the freestream velocity and the rotational velocity. Equations (5) and (6) show how the local velocity variation is expressed as a function of the freestream velocity and a non-dimensional weighting factor w based on advance ratio and radial position:

$$V_l^2 = V_\infty^2 + V_r^2 \tag{5}$$

$$\begin{aligned} V_l^2 &= V_\infty^2[1 + V_r^2/V_\infty^2] = V_\infty^2[1 + (2\pi nr)^2/V_\infty^2] \\ &= V_\infty^2[1 + (\pi r/JR)^2] \equiv V_\infty^2 w \end{aligned} \tag{6}$$

Elemental lift and drag forces, $\mathrm{d}L$ and $\mathrm{d}F_D$, are found using the local angle of attack, defined as the angle between the local blade chord line and the direction of the local flow V_l (Fig. 3). The elemental lift and drag are conventional in form but include the weighting factor w, accounting for the higher speeds near the tip in comparison to those closer to the hub, i.e.,

$$\mathrm{d}L = \frac{1}{2}\rho V_\infty^2 w c C_l \mathrm{d}r \tag{7}$$

$$\mathrm{d}F_\mathrm{D} = \frac{1}{2}\rho V_\infty^2 w c C_d \mathrm{d}r \tag{8}$$

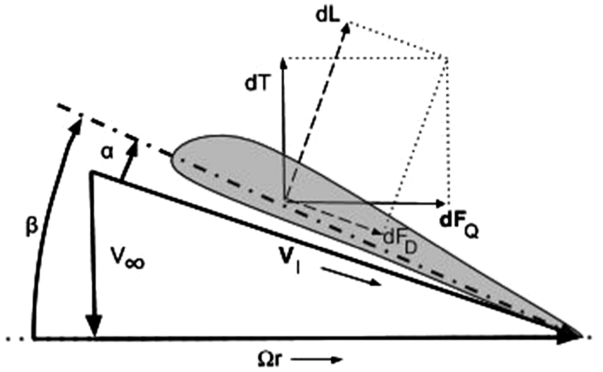

Fig. 3 Local blade-element flowfield and force components at a radial location *r*.

The resultant aerodynamic force on an element can also be decomposed into elemental thrust and circumferential forces: dT and $\mathrm{d}F_Q$. Elemental thrust is a function of the relevant components of elemental lift and drag, $\mathrm{d}L$ and $\mathrm{d}F_D$, and is written as

$$\mathrm{d}T = \frac{\Omega r}{V_l}\mathrm{d}L - \frac{V_\infty}{V_l}\mathrm{d}F_D = \left(\frac{\Omega r}{V_\infty}\mathrm{d}L - \mathrm{d}F_\mathrm{D}\right)\frac{1}{\sqrt{w}} \tag{9}$$

Overall thrust per blade is found by integrating from blade root to tip, i.e.,

$$T = \frac{1}{2}\rho V_\infty^2 \int_0^R \sqrt{w}\, c\left(C_l \frac{\Omega r}{V_\infty} - C_d\right)\mathrm{d}r \tag{10}$$

Similarly, elemental circumferential force is used to find torque per blade, i.e.,

$$Q = \frac{1}{2}\rho V_\infty^2 \int_0^R \sqrt{w}\, c\left(C_d \frac{\Omega r}{V_\infty} + C_l\right) r\,\mathrm{d}r \tag{11}$$

B. Characterization of the Pitching Moment

Of special interest in the PVPP concept is the blade pitching moment about the blade-pivot axis. The pivot axis is shown in schematic form in Fig. 4. Like thrust and torque, the blade pitching moment is found by integrating the contributions from each blade element. In developing the PVPP geometries used in this paper, the following procedure was used to ensure that the pivot axis lies on the local-section chord line or on the extended chord line for all radial stations of the blade. For any given airfoil and chord distributions for the blade, the pivot axis was placed at the correct fore-and-aft location on the untwisted blade geometry. The correct twist distribution was then applied by twisting each blade section about the blade-pivot axis. The methodology for determining the chord and twist distributions, and the methodology for the choice of the fore-and-aft position, are discussed in Sec. IV. For practical reasons, the blade-pivot axis is offset from the propeller axis, as shown in Fig. 4. This offset serves two purposes: first, the blade is more closely centered on the propeller axis, given that the blade-pivot axis is usually at a forward location on the blade; and second, the offset facilitates the simple mechanical synchronization of blade pitch for two-bladed propellers. The effects of blade-pivot offset on the airfoil lift, drag, and pitching moment are assumed to be negligible and are not included in the analysis in this paper.

The pitching moment about the blade-pivot axis is found by integrating the contributions from the various blade elements. As

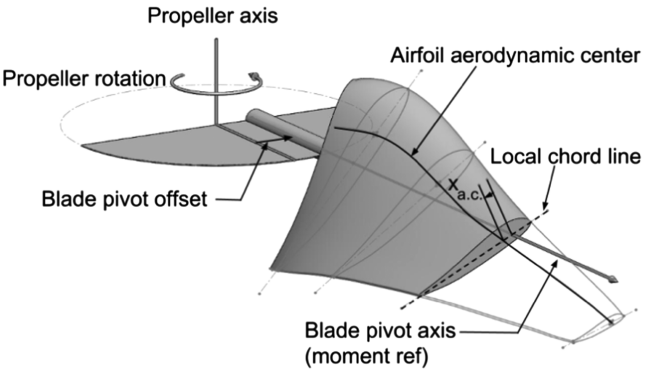

Fig. 4 Illustration showing blade-pivot offset and variation of local-section aerodynamic center along the radial direction of the propeller.

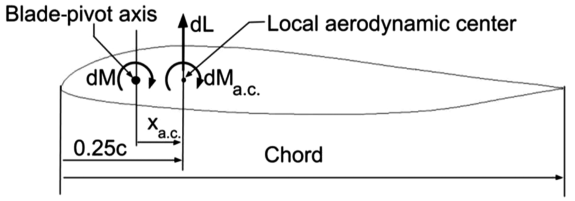

Fig. 5 Cross-section view of propeller blade showing contributions to the elemental moment about the blade-pivot axis.

shown in Fig. 5, the elemental contribution to the pitching moment about the blade pivot consists of two parts: the zero-lift pitching moment of the section $\mathrm{d}M_{\mathrm{a.c.}}$, and the moment produced by the elemental lift force $\mathrm{d}L$ acting over a moment arm $x_{\mathrm{a.c.}}$ from the blade-pivot axis to the local-section aerodynamic center. This gives

$$\begin{aligned}\mathrm{d}M &= \mathrm{d}M_{\mathrm{ac}} - \mathrm{d}L x_{\mathrm{ac}} \\ &= q_\infty w c^2 C_{m_{\mathrm{ac}}} \mathrm{d}r - q_\infty w c (C_{lo} + C_{l\alpha}\alpha) x_{\mathrm{ac}} \mathrm{d}r \end{aligned} \tag{12}$$

where α is the difference between the local chord line and the local inflow angle found using the advance ratio and radial location, i.e., $\alpha = \beta + \Delta\beta - \tan^{-1}(JR/\pi r)$. Integrating Eq. (12) across the blade gives the moment about the pitch axis:

$$M = q_\infty \int_0^R w c^2 C_{m_{\mathrm{ac}}} \,\mathrm{d}r - q_\infty \int_0^R w c x_{\mathrm{ac}} (C_{lo} + C_{l\alpha}\alpha)\,\mathrm{d}r \tag{13}$$

A PVPP blade must satisfy two conditions for static pitch stability about an equilibrium pitch angle, analogous to an aircraft in stable open-loop flight. First, the blade must have a pitching-moment equilibrium point at a positive-lift condition; and second, the blade pitch angle, upon being disturbed, must tend back to its equilibrium point. Equation (13) shows that, for the first condition, a lift-producing equilibrium point, defined by the zero pitching moment about the pivot axis (i.e., $M = 0$) requires either a positive (noseup) pitching moment about the airfoil aerodynamic center with the overall aerodynamic center located behind the pivot axis or a negative pitching moment about the aerodynamic center with the overall aerodynamic center position located forward of the pivot axis.

The second condition is a restoring moment given a pitch disturbance. To better understand this condition, the pitching moment expression from Eq. (13) is written in terms of β, $\Delta\beta$, and the advance ratio J, i.e.,

$$\begin{aligned}M = {} & q_\infty \int_0^R w c^2 C_{m_{\mathrm{ac}}} \,\mathrm{d}r - q_\infty \int_0^R w c x_{\mathrm{ac}} C_{lo}\,\mathrm{d}r \\ & - q_\infty \int_0^R w c x_{\mathrm{ac}} C_{l\alpha} \left(\beta + \Delta\beta - \tan^{-1}\left(\frac{JR}{\pi r}\right)\right) \mathrm{d}r \end{aligned} \tag{14}$$

The derivative of pitching moment with α, assuming constant J and neglecting induced-flow changes, is

The

$$\frac{\mathrm{d}M}{\mathrm{d}\alpha} = \frac{\mathrm{d}M}{\mathrm{d}(\Delta\beta)} = -q_\infty \int_0^R w c x_{\mathrm{ac}} C_{l\alpha}\,\mathrm{d}r \tag{15}$$

To generate a restoring moment upon perturbation, as well as meet the second condition for static stability, Eq. (15) indicates that the overall aerodynamic center for the blade must be placed downstream of the blade-pivot axis. Under the further assumption of a constant lift-curve slope, the following expressions are obtained:

$$\begin{aligned}\frac{\mathrm{d}M}{\mathrm{d}\alpha} &= -\frac{(q_\infty C_{l\alpha} \int_0^R w c\,\mathrm{d}r)}{\int_0^R w c\,\mathrm{d}r} \int_0^R w c x_{\mathrm{ac}}\,\mathrm{d}r \\ &= -\frac{\mathrm{d}L/\mathrm{d}\alpha}{\int_0^R w c\,\mathrm{d}r} \int_0^R w c x_{\mathrm{ac}}\,\mathrm{d}r \end{aligned} \tag{16}$$

$$\begin{aligned}\frac{\mathrm{d}M/\mathrm{d}\alpha}{\mathrm{d}L/\mathrm{d}\alpha} &= -\frac{1}{\int_0^R w c\,\mathrm{d}r} \int_0^R w c x_{\mathrm{ac}}\,\mathrm{d}r \\ &= -\frac{1}{S'} \int_0^R w c x_{\mathrm{ac}}\,\mathrm{d}r \end{aligned} \tag{17}$$

The integral

$$\int_0^R w c\,\mathrm{d}r$$

represents a weighted planform area, denoted by S', which takes into account the higher speeds at the outboard sections of the blade. The numerator is a similarly weighted average location of the aerodynamic center of the blade. The formulation mirrors the standard form for a three-dimensional wing aerodynamic center [10,11], but it appropriately weights the outboard sections of the blade by a factor equal to the increase in dynamic pressure from propeller rotation and is denoted

$$X'_{\mathrm{ac}} = \frac{-\mathrm{d}M}{\mathrm{d}L} = \frac{1}{S'} \int_0^R w c x_{\mathrm{ac}}\,\mathrm{d}r \tag{18}$$

If a base condition is chosen where the lift coefficient is relatively constant along the blade and the pitching moment about the local aerodynamic center is assumed constant along the blade, the lift and moment equations can be reduced into a form similar to those used in wing aerodynamics. Examining the lift of the airfoil under the stated assumptions and incorporating the definition of weighted planform area from Eq. (7) yields

$$\begin{aligned}L &= q_\infty \int_0^R w c C_l\,\mathrm{d}r = q_\infty C_L \int_0^R w c\,\mathrm{d}r \\ &= q_\infty C_L S' \end{aligned} \tag{19}$$

Approaching the pitching moment in a similar fashion and starting with Eq. (13) gives

$$\begin{aligned}M &= q_\infty \int_0^R w c^2 C_{m_{\mathrm{ac}}}\,\mathrm{d}r - q_\infty \int_0^R w c C_l x_{\mathrm{ac}}\,\mathrm{d}r \\ &= q_\infty C_{m_{\mathrm{ac}}} \int_0^R w c^2\,\mathrm{d}r - q_\infty C_L \int_0^R w c x_{\mathrm{ac}}\,\mathrm{d}r \\ &= q_\infty C_{m_{\mathrm{ac}}} \int_0^R w c^2\,\mathrm{d}r - q_\infty C_L X'_{\mathrm{ac}} S' \end{aligned} \tag{20}$$

The blade mean aerodynamic chord $\bar{c}'$ is found in a similar fashion as for a standard wing and is defined as the chord of a constant-chord blade of the same span and planform area that produces the same pitching moment. Using this definition of mean aerodynamic chord, the pitching moment for a constant-chord blade is

$$M_{\text{const chord}} = q_\infty C_{m_{\text{ac}}} \bar{c}' \int_0^R wc \, \mathrm{d}r - q_\infty C_L \int_0^R wcx_{\text{ac}} \, \mathrm{d}r$$
$$= q_\infty C_{m_]} \bar{c}' S' - q_\infty C_L X'_{\text{ac}} S' \tag{21}$$

$$M_{\text{const chord}} = q_\infty \bar{c}' S' \left(C_{m_{\text{ac}}} - C_L \frac{X'_{\text{ac}}}{\bar{c}'} \right) \tag{22}$$

Equating the constant-chord moment from Eq. (22) with the general geometry moment from Eq. (20) results in Eq. (23), giving the definition of a weighted mean aerodynamic chord for the blade in Eq. (24):

$$\int_0^R wc^2 \, \mathrm{d}r = \bar{c}' S' \tag{23}$$

$$\bar{c}' = \frac{\int_0^R wc^2 \, \mathrm{d}r}{S'} \tag{24}$$

Equation (24) resolves the integral

$$\int_0^R wc^2 \, \mathrm{d}r$$

in the pitching moment equation [Eq. (20)] and helps derive a compact expression for the static margin of a blade. This expression, given in Eq. (25), is found to be identical to that used in wing/aircraft aerodynamics, albeit with modified planform constants:

$$SM' = \frac{-\mathrm{d}C_M}{\mathrm{d}C_L} = \frac{X'_{\text{ac}}}{\bar{c}'} \tag{25}$$

As with conventional use in aircraft aerodynamics, this static margin is a measure of the pitch stiffness of the PVPP blade. For a statically stable system, the variation of pitching moment with lift must have a negative slope, yielding a positive static margin. It must be noted that, unlike a conventional planform, static margin is not constant over a range of operating conditions, but it is valid only for the advance ratio used in the calculation. Additionally, the derivations shown in this section are limited by the assumption of negligible contributions from the induced-inflow velocities. Static margins under general conditions with inflow contributions must be calculated numerically by solving for blade conditions and using finite differences to calculate the slope of the $\mathrm{d}C_M/\mathrm{d}C_L$ curve.

III. Computational Modeling

A. Aerodynamic Analysis

Two available propeller codes were considered as a basis for analysis of the PVPP concept. The first is QPROP [12,13]. This code employs an extension of the classic blade-element/vortex formulation and accounts for both the induced axial flow and the swirl components of flow along the blade. QPROP takes as input the linear variation for C_l vs α and a two-part quadratic variation for C_d vs α, both with defined ranges. Estimates for changes to coefficients from the Reynolds number and compressibility effects may also be included. The second code uses a blade-element model coupled with a momentum calculation [14]. The induced flow is modeled as purely axial and is set as radially uniform or varying. To determine the propeller performance, the code uses drag polars for blade cross sections at various Reynolds numbers. Although experimental polars would be best, finding data for the blade-cross-section airfoils at the Reynolds numbers relevant to small-UAV-sized propellers is not always practical. In this work, the XFOIL code [15] was used to estimate the lift and drag characteristics. Figure 6 compares results from the two codes for the Graupner 10×8 Cam Slim propeller with experimental data from tests conducted at the NASA Langley Basic Aerodynamic Research Tunnel (BART) [14]. Both codes match experimental data and each other fairly well. However, QPROP was selected as the code for further analysis because it includes the calculation of swirl effects.

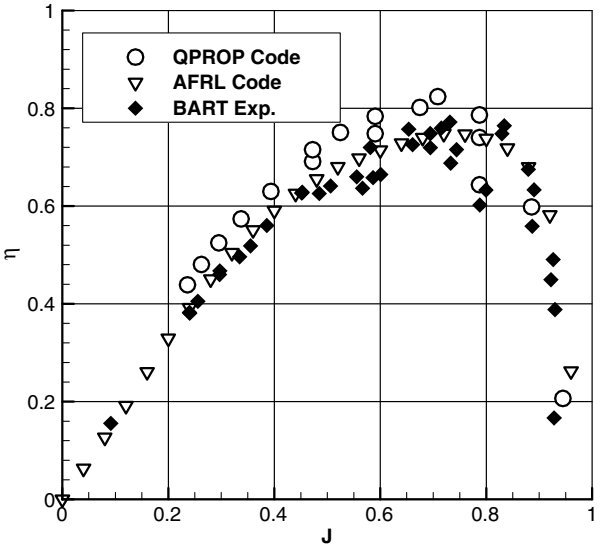

Fig. 6 Comparison of computational and experimental performance for the Graupner 10×8 Cam Slim propeller. Experimental data are from [14].

An essential capability to analyze the PVPP concept is a code that can perform the pitching-moment calculation and that can iterate on the blade pitch angle $\Delta\beta$ to find the pitching-moment equilibrium point. A code, named PVQPROP, with the desired functionality was assembled using QPROP as a base, modified to include pitching-moment calculations and an outer loop to iterate on blade pitch angle $\Delta\beta$. This capability was achieved by inserting the calculation of the pitching moment from Eq. (13) to find the moment on the blade. Inputs were expanded to include C_{mo} and $\mathrm{d}C_m/\mathrm{d}C_l$ distributions along the blade. The C_{mo} value was determined by airfoil type, and the $\mathrm{d}C_m/\mathrm{d}C_l$ value was calculated using the defined x_{ac} and the local blade-element chord and lift. As a first test of the PVPP concept using the PVQPROP code, the Graupner 10x8 Cam Slim propeller geometry, tested by the U.S. Air Force Research Laboratory (AFRL) [14], was chosen as the test case. Drag polars used in the AFRL analysis were used to find necessary linear and quadratic aerodynamic coefficients. Airfoil pitching-moment characteristics, representative of a reflexed airfoil, corresponding to a C_{mo} value of 0.04 and $\mathrm{d}C_m/\mathrm{d}C_l$ value of -0.08 were used, yielding a two-dimensional airfoil equilibrium lift coefficient of 0.5.

The propeller geometry was first analyzed with the QPROP code at a variety of fixed $\Delta\beta$ angles yielding a family of curves. The same propeller geometry, used as a PVPP, was then analyzed using PVQPROP over a range of advance ratios with the $\Delta\beta$ outer loop solving for equilibrium blade angles through a Newton iteration on pitching moment. Figure 7 compares the results from both cases and highlights the envelope expansion potential of the PVPP. Figure 8 compares the predicted propeller efficiency vs advance ratio for the PVPP with the experimental data from [14] for the fixed-pitch Graupner 10×8 Cam Slim propeller. Also shown in Fig. 8 is the predicted variation of $\Delta\beta$ with the advance ratio. The results indicate that, over the specified range of advance ratios from 0 to 2, the blades rotate from an equilibrium pitch angle of -15 to 24 deg. The simulated PVPP maintains efficiencies near the peak of an appropriately matched fixed-pitch propeller over the entire range. Although there is no significant efficiency improvement at low advance ratios, the simulated PVPP is seen to have good efficiencies,

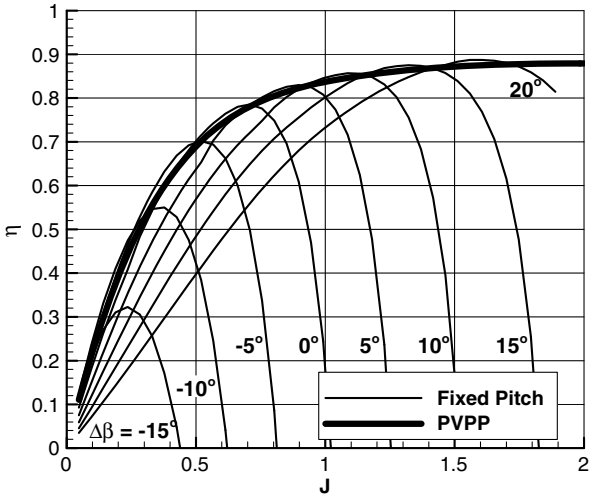

Fig. 7 Predicted efficiency curves for the Graupner 10 × 8 Cam Slim propeller geometry at a range of fixed blade pitch angles compared to the same geometry as a PVPP.

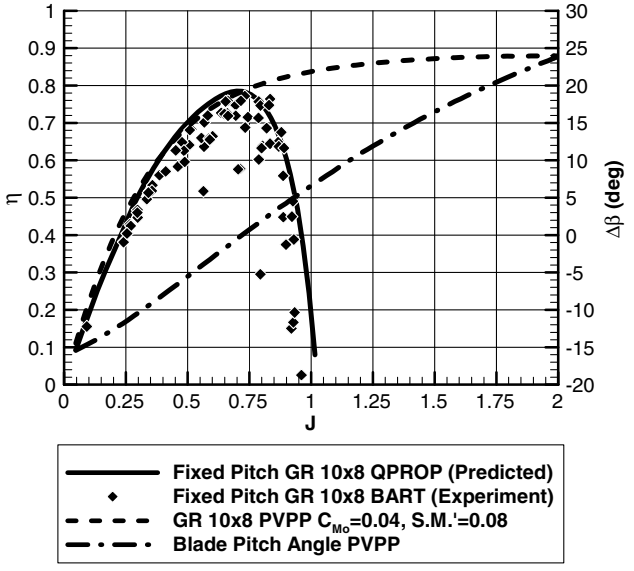

Fig. 8 Graupner (GR) 10 × 8 Cam Slim PVPP performance compared to fixed-pitch computational and experimental data. Experimental data are from [14].

of 0.85–0.9, across a broad range of higher advance ratios, which is a significant improvement over the fixed-pitch propeller.

B. Modeling of Static and Dynamic Imbalance Effects

Conceptually, the PVPP leverages purely aerodynamic moments to achieve and maintain equilibrium blade pitch angles. To achieve this aerodynamic equilibrium, pitching moments from mass effects must be minimized through careful mass balancing. The coupling between blade pitching moments and mass/inertia properties is examined by considering a single blade, shown in Fig. 9. The inertial frame is denoted by I_{XYZ}, labeled "INERTIAL," and, by definition, is a nonrotating frame. This frame is placed such that the X axis is coincident with the propeller axis of rotation, and the $Y-Z$ plane contains the blade-pivot axis. At the time instant of interest in the following discussion, it is assumed that the blade-pivot axis is parallel to the inertial Z axis. The second reference frame is denoted by $B_{X'Y'Z'}$ and labeled "BLADE." This frame is fixed to the blade with the origin located on the blade-pivot axis such that the Z location of the origin of this frame is at the Z location of the blade center of gravity (CG) location. The inertial coordinates of the origin of the

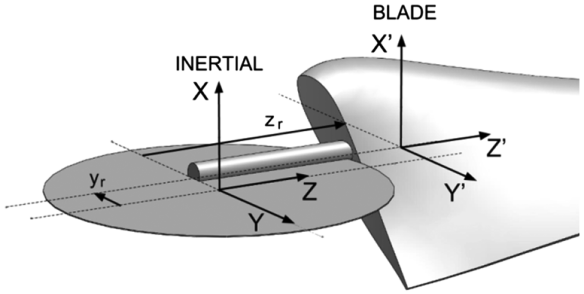

Fig. 9 Inertial and blade reference frames showing pivot axis offset from propeller axis of rotation. As shown in this figure, y_r is negative.

blade frame are $(0, y_r, z_r)$. When the blade pitch angle is at its predesignated reference value, the blade X' and Y' axes are parallel to the inertial X and Y axes, respectively. Positive changes to the blade pitch angle (from the reference value) by $\Delta\beta$ will result in positive rotation of the BLADE frame about the Z' axis by $\Delta\beta$.

If the blade is statically balanced, the blade CG will fall on the blade pitch pivot axis, and it will therefore coincide with the origin of the BLADE frame. For a blade with static imbalance, the coordinates of the CG in the blade frame, which are independent of $\Delta\beta$, are denoted by $(\Delta X', \Delta Y', 0)$, resulting in position vector from blade origin to the CG $\boldsymbol{BCG}$ expressed in the blade frame as

$$\boldsymbol{BCG}_{\text{BLADE}} = (\Delta X', \Delta Y', 0) \tag{26}$$

and expressed in the inertial frame as

$$\boldsymbol{BCG}_{\text{INERTIAL}} = (\Delta X' \cos\Delta\beta - \Delta Y' \sin\Delta\beta, \Delta X' \sin\Delta\beta + \Delta Y' \cos\Delta\beta, 0) \tag{27}$$

The position vector from inertial origin to the blade CG as expressed in the inertial frame is

$$\boldsymbol{ICG}_{\text{INERTIAL}} = (\Delta X' \cos\Delta\beta - \Delta Y' \sin\Delta\beta, y_r + \Delta X' \sin\Delta\beta + \Delta Y' \cos\Delta\beta, z_r) \tag{28}$$

The effects of static and dynamic imbalance are considered at conditions when the blade is in pitch equilibrium; at this condition, the angular velocity of the blade from blade pitch about the pivot axis is zero, i.e., $\partial\Delta\beta/\partial t = 0$. Therefore, the only angular velocity of the system is that from propeller rotation about the propeller axis, which is also the angular velocity of the blade frame relative to the inertial frame. This angular velocity expressed in the inertial frame is $\boldsymbol{\omega}_{\text{INERTIAL}} = (\Omega, 0, 0)$, and expressed in the blade frame, for nonzero $\Delta\beta$, is $\boldsymbol{\omega}_{\text{BLADE}} = (\Omega\cos\Delta\beta, -\Omega\sin\Delta\beta, 0)$. The contribution to the blade pitching moment about the blade-pivot axis from static imbalance results from the blade CG being offset from the blade-pivot axis. This pitching moment is the moment from the centrifugal force acting over the moment arm due to offset of the CG from the blade-pivot axis. The centripetal force, expressed in the inertial frame is

$$\boldsymbol{F}_{\text{INERTIAL}} = m(\boldsymbol{\omega}_{\text{INERTIAL}} \times (\boldsymbol{\omega}_{\text{INERTIAL}} \times \boldsymbol{ICG}_{\text{INERTIAL}})) \tag{29}$$

where m is the entire mass of a single blade. The magnitude of the resulting moment (from static imbalance) about the blade-pivot axis (which is aligned with the Z' axis) is

$$M_{\text{static}} = (\boldsymbol{BCG}_{\text{INERTIAL}} \times -\boldsymbol{F}_{\text{INERTIAL}}) \cdot \hat{k} \tag{30}$$

which, on expansion, becomes

$$M_{\text{static}} = m\Omega^2(\Delta X' \cos\Delta\beta - \Delta Y' \sin\Delta\beta)(y_r + \Delta X' \sin\Delta\beta + \Delta Y' \cos\Delta\beta) \quad (31)$$

The second contribution to pitching moment about the blade pivot occurs as a result of dynamic imbalance. This contribution can be related to the rate of change of angular momentum of the blade [16]. As discussed in [16], Eq. (32) shows that the net external moment (about the origin of the BLADE frame) applied to the rotating blade is equal to the rate of change in absolute angular momentum about the origin of the BLADE frame. The right side of Eq. (32) has two terms because the rate of change in angular momentum here is written in the coordinates of the rotating blade frame, i.e.,

$$\boldsymbol{M}_{\text{BLADE}} = (\dot{\boldsymbol{H}}_{\text{BLADE}})_{X'Y'Z'} + \boldsymbol{\omega}_{\text{BLADE}} \times \boldsymbol{H}_{\text{BLADE}} \quad (32)$$

Of interest in the current work is the moment about the pivot axis, which is aligned with the Z' axis. Expanding only the Z' component of the $\boldsymbol{M}_{\text{BLADE}}$ component yields

$$M_{Z'} = I_{Z'Z'}\dot{\omega}_{Z'} - (I_{X'X'} - I_{Y'Y'})\omega_{X'}\omega_{Y'} - I_{Z'X'}(\dot{\omega}_{X'} - \omega_{Y'}\omega_{Z'}) - I_{X'Y'}(\omega_{X'}^2 - \omega_{Y'}^2) - I_{Y'Z'}(\dot{\omega}_{Y'} + \omega_{Z'}\omega_{X'}) \quad (33)$$

where the inertia terms are defined similar to $I_{X'X'} = \int(Y'^2 + Z'^2)\,\mathrm{d}m$ and $I_{X'Y'} = \int X'Y'\,\mathrm{d}m$.

For steady-state operation, the time derivatives go to zero. Further, because angular velocity results only from propeller rotation, $\boldsymbol{\omega}_{\text{BLADE}} = (\Omega\cos\Delta\beta, -\Omega\sin\Delta\beta, 0)$; the Z' component of $\boldsymbol{\omega}_{\text{BLADE}}$ goes to zero. The moment about the pivot axis due to dynamic imbalance is $-M_{Z'}$, which can be written as

$$M_{\text{dynamic}} = -M_{Z'} = (I_{X'X'} - I_{Y'Y'})\omega_{X'}\omega_{Y'} + I_{X'Y'}(\omega_{X'}^2 - \omega_{Y'}^2) \quad (34)$$

These static and dynamic imbalance contributions indicate that, to achieve pure aerodynamic pitch equilibria, two conditions must be met. First, the blade center of gravity must be placed on the blade-pivot axis. Second, the product of inertia in the plane normal to blade pitch must be balanced to zero, and the moments of inertia about the blade-frame X' and Y' axes must equal one another. If the blade is not balanced, the sum of moments [from Eqs. (31) and (34)] must be added to aerodynamic moments, resulting in changes to the equilibrium pitch angle of the blade and in changes to the blade static margin.

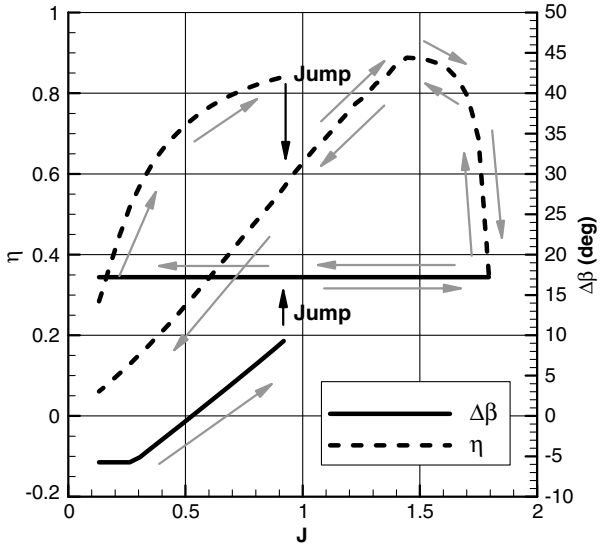

Fig. 10 Simulation of an example PVPP configuration showing typical hysteresis behavior caused by static imbalance.

The moment contributions from the static and dynamic imbalance [Eqs. (31 and 34)] were incorporated into the PVQPROP code to enable modeling of the PVPP behavior in the presence of such imbalance. If the effects of imbalance overpower those due to aerodynamics, the resulting moments can cause the propeller blades to pitch, up or down, to the mechanical stops. Additionally, given the dependency of the moment on blade pitch angle, inertial effects may be present as a hysteresis effect in which aerodynamic effects are initially dominant, but imbalance effects increase with blade pitch until they dominate the aerodynamic moments and cause the propeller pitch to reach and stay at a mechanical stop. An example of such a hysteresis behavior from PVQPROP simulation is shown in Fig. 10 for a blade with static imbalance. In this example, a PVPP is simulated with an advance ratio gradually increasing from a low value of 0.1. Initially, the blade pitch angle $\Delta\beta$ increases in response to the increase in advance ratio. At $J = 0.9$, the blade experiences a sudden increase in pitch angle to the maximum limit (simulated mechanical stop). Subsequently, any increase or decrease in advance ratio has no effect on the pitch angle, which remains at the maximum limit. Similar hysteresis behavior was also observed when PVPP blades were simulated with dynamic imbalance from a nonzero $I_{X'Y'}$. This example illustrates the adverse effect of imbalance on the behavior of the PVPP and shows the importance of statically and dynamically balancing the propeller blades.

IV. Development of a Candidate Test Propeller

To begin test propeller development, an Eppler 325 reflexed airfoil (coordinates available from [17]) was chosen for the base candidate airfoil. This airfoil combines the desired pitching-moment characteristics, a not overly thin trailing edge, and a relatively thick forward section, which were necessary from a design and construction point of view. The airfoil was modified by increasing the thickness ratio by 20%, from 12.6 to 15.12%c for pivot-shaft installation, and further thickening the trailing edge along the blade to 0.03 in. for construction considerations. Figure 11 shows the modified airfoil. The required aerodynamic coefficients for the modified airfoil were then generated using the XFOIL code. Because of the relatively low operational propeller blade Reynolds numbers, boundary-layer transition was forced on the upper and lower surfaces of the airfoil at 20 and 60%, respectively, corresponding to the planned placement of trips on the test propeller. The forced-transition locations were determined through a trial-and-error process using the XFOIL code, with the aim of minimizing the effects of the laminar separation bubble on the upper surface and the laminar separation on the aft portion of the lower surface. The XFOIL analysis yielded $C_{l\alpha=0} = -0.0801$, $C_{l\alpha} = 6.76$ /rad, and $C_{mo} = 0.0626$. The remaining necessary parameter, $C_{m\alpha}$, is dependent on $x_{\text{a.c.}}$, which is the local distance between the aerodynamic center of the airfoil and the pivot axis of the blade.

The candidate propeller twist and chord distribution was generated using the QMIL utility, packaged with the QPROP code. This utility, given desired performance, generates geometry for the minimum induced loss condition [18–20]. The algorithm imposes a user-defined lift-coefficient constraint and then solves for the chord and pitch distributions to generate the requisite thrust at the given propeller rotations per minute (RPMs). The inverse design with QMIL was performed for a propeller with two blades and a 20 in. diameter to produce 4.5 lb of thrust at 4000 RPMs and 60 ft · s^{-1}. After the chord and sweep distributions were generated, the propeller

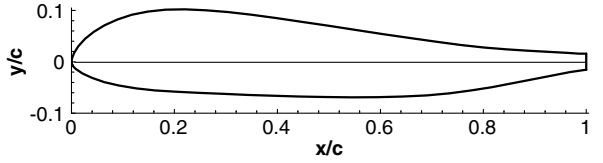

Fig. 11 E325 airfoil geometry modified to facilitate propeller blade construction.

diameter was trimmed to 18 in. to avoid a very small, thin tip. The blade-pivot offset was set to 0.5 in., or 0.056 R, to allow for synchronization of the blade pitch angles using readily available hardware.

Aerodynamic center $x_{\text{a.c.}}$ distribution was used as a further design parameter to allow for some tailoring of offdesign PVPP performance. This tailoring is possible because of the dependency of the spanwise lift distribution on advance ratio. Although blade twist is fixed by the initial propeller design, spanwise inflow angles change continuously with advance ratio. Given an increase in the advance ratio, the increase in inflow angle at the root is much larger than at the tips, which serves to unload the inboard section of the propeller relative to the outboard sections. If the $x_{\text{a.c.}}$ distribution is tailored such that $\mathrm{d}C_m/\mathrm{d}C_l$ is held constant along the blade, it may result in little more than a loading redistribution of the blade. However, if the blade is swept aft, the $x_{\text{a.c.}}$ of the tip is significantly higher than those for the inboard sections. The loading shift to the tips with the higher $x_{\text{a.c.}}$ yields an increase in nosedown pitching moment, causing a lower overall blade equilibrium pitch angle.

Using Eqs. (18) and (25), which define the $X'_{\text{a.c.}}$ and SM' of the propeller, a spreadsheet tool was developed that uses QMIL-generated chord and twist distributions, as well as a user-specified $x_{\text{a.c.}}$ distribution, to yield the planform geometry of the propeller and the blade-shaft location (relative to this planform geometry) for a desired blade static margin. The $x_{\text{a.c.}}$ distribution is parameterized by choosing a percent airfoil chord to be held straight (parallel to the pivot axis). For a blade with the zero-percent-chord held straight, the leading edge would appear unswept, whereas a blade with the 100% chord held straight would have an unswept trailing edge. After setting the $x_{\text{a.c.}}$ distribution, local $-\mathrm{d}C_m/\mathrm{d}C_l$ is found using local aerodynamic center position, chord, and location of the blade-pivot point for a given SM'. Figure 12 shows example geometries resulting from 20, 50, and 80%c lines held straight with SM' set to 0.12 (or 12%). In each plot, the heavy black line indicates the untwisted chord distribution of the planform, and the lighter line shows the projected planform after blade twist is added. The radial distribution of the local-section aerodynamic center is shown using the small-dashed curve. The overall blade aerodynamic center, found through blade-element integration from Eq. (18), is indicated by the dashed–dotted line. The blade-pivot axis, which is set forward of the overall blade aerodynamic center by the desired SM' of 12%, is indicated by the heavy-dashed line. The blade-pivot axis is offset from the propeller axis of rotation, which is at (0, 0) in the plots in Fig. 12, by 0.5 in. to accommodate synchronizing gears.

Using the same chord and twist distributions, geometries were generated for $x_{\text{a.c.}}$ distributions resulting from 50%c straight, 80%c straight, and 100%c straight, as well as for SM' of 7 and 12%. The resulting efficiency plots, shown in Figs. 13–15 from PVQPROP predictions, assuming statically and dynamically balanced blades, were similar in nature to the previous computational test case using the Graupner propeller geometry (Figs. 7 and 8). The blade equilibrium pitch angle is seen to adjust with varying advance ratios, which expands the advance-ratio range for high efficiency as compared to that for the fixed-pitch propeller. The unloading behavior from $x_{\text{a.c.}}$ and the effect of the design static margin are indicated in the variation of $\Delta\beta$ with the advance ratio. Comparing the three $x_{\text{a.c.}}$ distribution cases, it is noted that, as the percent chord held straight is shifted aft, the increased loading of the blade tips causes the blade to trim to smaller angles as the advance ratio increases. For all three $x_{\text{a.c.}}$ distributions, the lower static margin blades trimmed to higher pitch angles, corresponding to higher loading cases. The variation of effective static margin, found computationally using finite difference (and plotted as a function of J in Figs. 13–15) can also be compared to the design static margin. This shows that, as the constant percent chord line is shifted aft, the effective static margin tends to be higher than the design static margin, especially at low advance ratios, and it shifts toward the design value as the advance ratio increases.

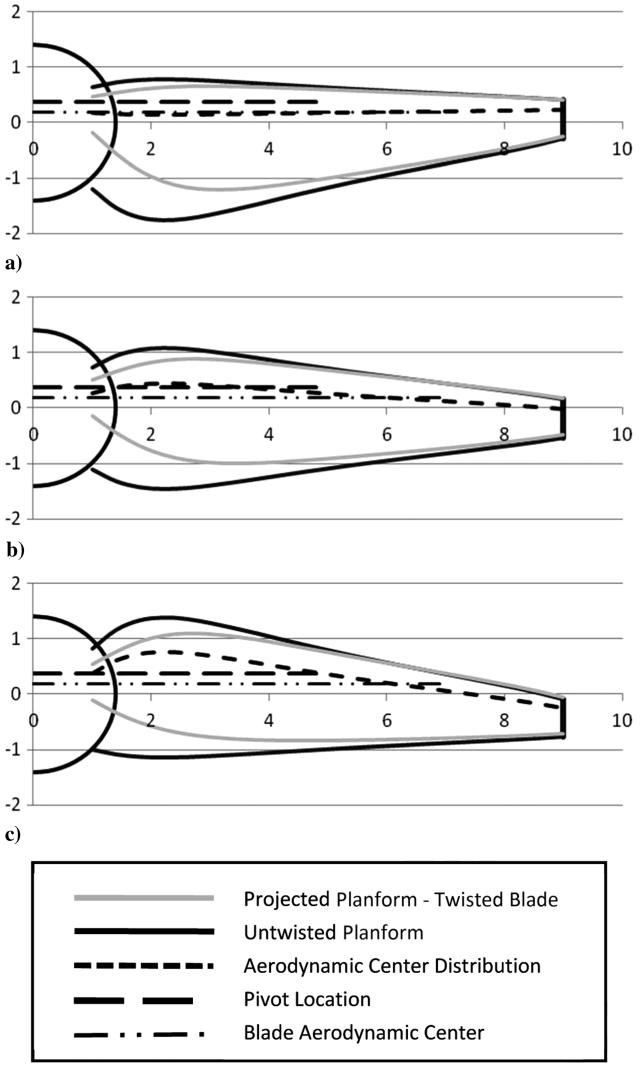

Fig. 12 Example propeller geometries (propeller rotation counterclockwise) with blade sweep angles defined by percent chord lines held straight: a) 20%c straight, b) 50%c straight, and c) 80%c straight. Dimensions are in inches.

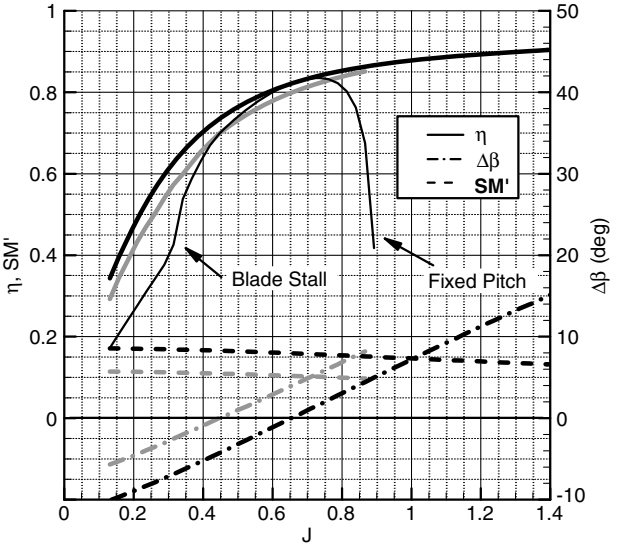

Fig. 13 Predicted performance for two PVPPs (7% or 0.07 SM' in gray, and 12% or 0.12 SM' in black) with the 50% chord line held straight compared with fixed pitch ($\Delta\beta = 0$).

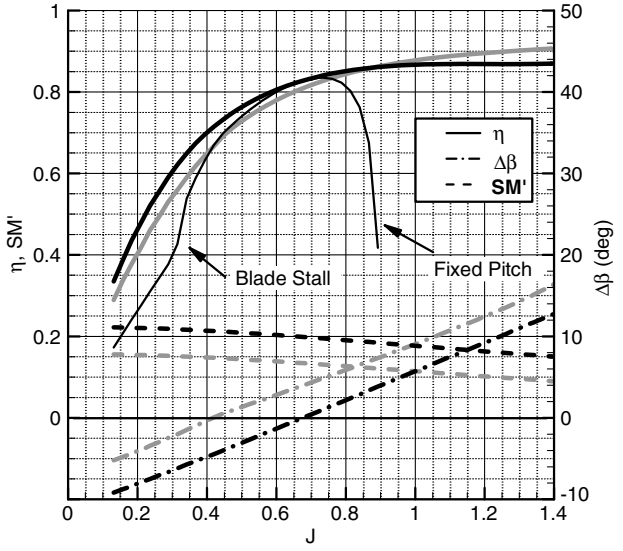

Fig. 14 Predicted performance for two PVPPs (7% or 0.07 SM' in gray, and 12% or 0.12 SM' in black) with the 80% chord line held straight compared with fixed pitch ($\Delta\beta = 0$).

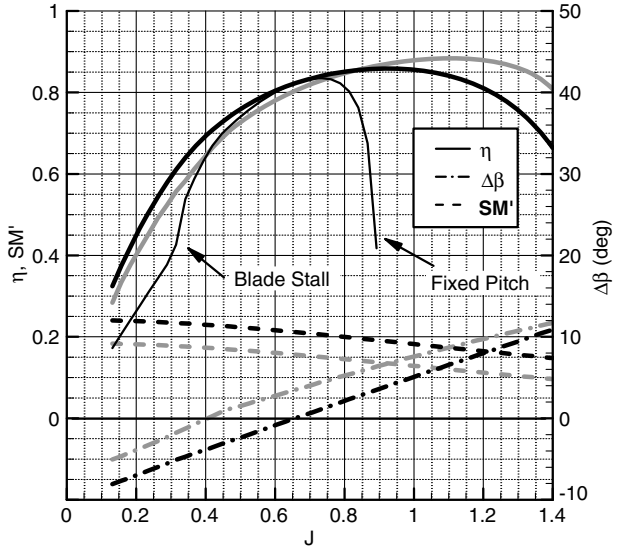

Fig. 15 Predicted performance for two PVPPs (7% or 0.07 SM' in gray, and 12% or 0.12 SM' in black) with the 100% chord line held straight compared with fixed pitch ($\Delta\beta = 0$).

Performance variation with $x_{\text{a.c.}}$ distribution can be better understood by examining blade lift distributions. Figure 16 shows the local α distributions along the blade for three cases: 10%c held straight, 50%c held straight, and 80%c held straight. The spanwise alpha distribution for the 10%c case reveals that, for this case, the increase in advance ratio causes the inboard blade section to unload and the outboard to load, such that the overall C_L is changed only slightly (Fig. 16a). When the code is run with the blade $x_{\text{a.c.}}$ defined by 50 or 80%c lines held straight, with increase in advance ratio, the off-design loading is reduced (Figs. 16b and 16c).

To demonstrate the potential impact of sweep on the propeller-motor matching exercise, several propeller geometries were designed and analyzed in combination with a hypothetical electric motor. The electric motor specifications were set to be roughly representative of a motor that would be used to drive a 1.5-ft-diam propeller. Electrical limits were set to maximums of 37 V DC and 75 A. The typical brushless motor has some proportionality between supply voltage and rotational speed, generally listed for each motor as K_v in units of

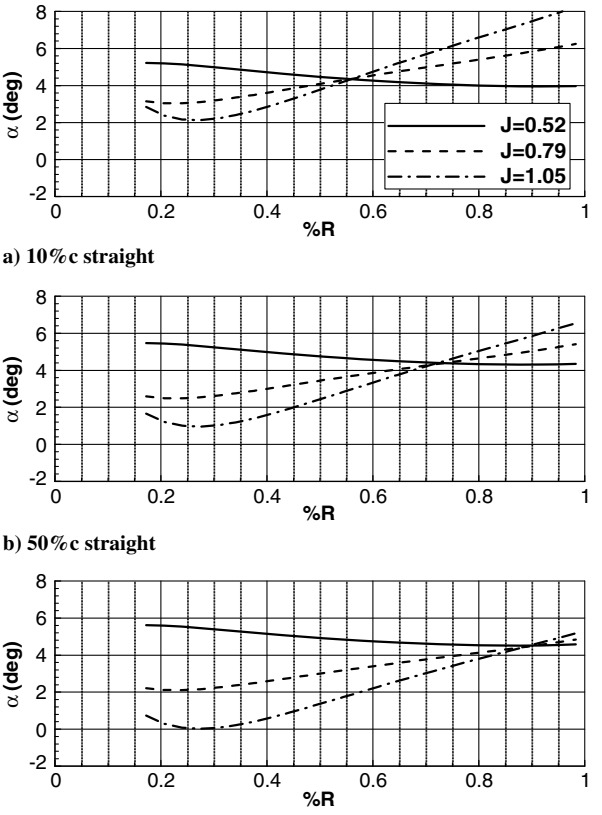

Fig. 16 Effect of the advance ratio on angle-of-attack distribution for three $x_{\text{a.c.}}$ distributions.

RPM/volt. Further, the motor speed control is limited by how much current it can source without either tripping a safety cutoff or resulting in heat damage to the controller or motor. For the purposes of this study, the propeller is limited by one or the other of these constraints.

Two propeller geometries were studied, corresponding to sweeps of 80%c straight and 100%c straight. These geometries were each studied for static margins of 9 and 12%, along with fixed-pitch cases set at fixed $\Delta\beta$ angles of 0 and -8 deg. Figure 17 shows that all the PVPP cases are predicted to have significantly better thrust at low-speed conditions as compared to the fixed-pitch propeller at a 0 deg $\Delta\beta$. The fixed-pitch propeller with -8 deg $\Delta\beta$ produces thrust comparable to the PVPPs at low speeds but, as velocity increases, the PVPP models allow the blades to adjust to increased advance ratio and maintain thrust, whereas the fixed-pitch propeller quickly overspeeds and no longer produces thrust.

V. Wind-Tunnel Experimental Results and Comparison to Computational Results

Prototype two-blade PVPPs were fabricated for experimental testing in the North Carolina State University (NCSU) low-speed wind tunnel. The wind tunnel is a closed-circuit tunnel capable of dynamic pressures to approximately 20 lb · ft^{-2}. The tunnel test section is 43 in. wide, 33 in. high, and 48 in. long. Turbulence levels were 0.5–0.6%. The PVPP prototypes were tested both in free-to-pitch mode and in fixed-pitch mode, with the pitch angle locked at various values. The experimental results in this section are compared to those predicted by the PVQPROP code (described in Sec. III).

Test propeller blades were based on the candidate propeller geometry described previously. Two molds of 80%c straight geometry were rapid prototyped: the first with a 12% static margin (denoted 8012) and the second with a 9% static margin (denoted 8009). The molds were designed with a channel to allow installment and alignment of the blade shaft, as well as sockets to key the two halves of the mold accurately. The blades were constructed using a

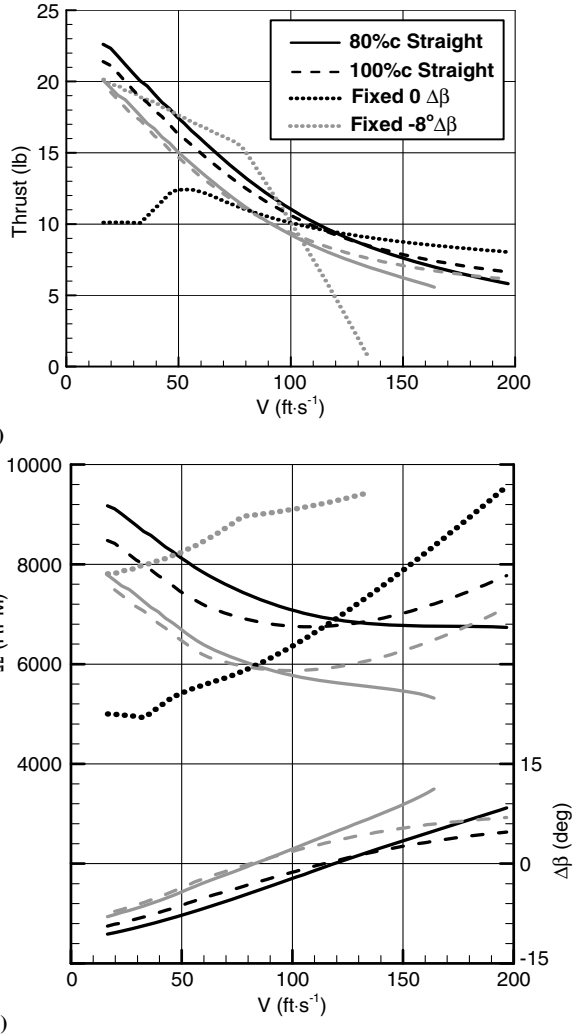

Fig. 17 Motor-matched propeller performance for 80 and 100%c lines held straight at two static margins, 9% (gray) and 12% (black): a) thrust performance; and b) propeller speed and blade pitch angle.

wet layup technique from Fiberglas and unidirectional carbon fiber in two halves. After trimming and prepping the two halves of each blade, they were joined with the shaft bonded in place. Shafts were fabricated from case-hardened stainless stock. Figure 18 shows an example propeller blade with the molds used for fabrication.

After the blades were bonded and cleaned, the roots were trimmed to match the 3.5 in. spinner hub and checked for clearance. Boundary-layer trips were added at 20%c on the upper surface and 60%c on the lower, corresponding to forced-transition locations used for the XFOIL analysis. The weight of each blade, without the stainless shafts, fell under 0.53 oz.

Using the measured values, solid models of the 8009 and 8012 blades were updated to reflect the as-built weights of the test articles. Each blade was mounted on a Dubro Tru-spin Prop Balancer, using the blade shaft, and mass balanced, using adjustable masses in the propeller hub as shown in Fig. 19, to place the CG on the blade-pivot axis. Once the CG was correctly balanced, the solid model mass properties were again updated, and the amount of mass to minimize $I_{X'Y'}$ and $(I_{X'X'} - I_{Y'Y'})$ was found computationally. The resulting inertia matrix for blade and mass balancing, taken at the blade CG (origin of the blade frame) and aligned with X', Y', Z' for the 8009, was

$$I(X', Y', Z') = \begin{bmatrix} 7.41 & 0.00 & -0.38 \\ 0.00 & 7.41 & 0.68 \\ -0.38 & 0.68 & 0.57 \end{bmatrix} \text{ oz} \cdot \text{in}^2$$

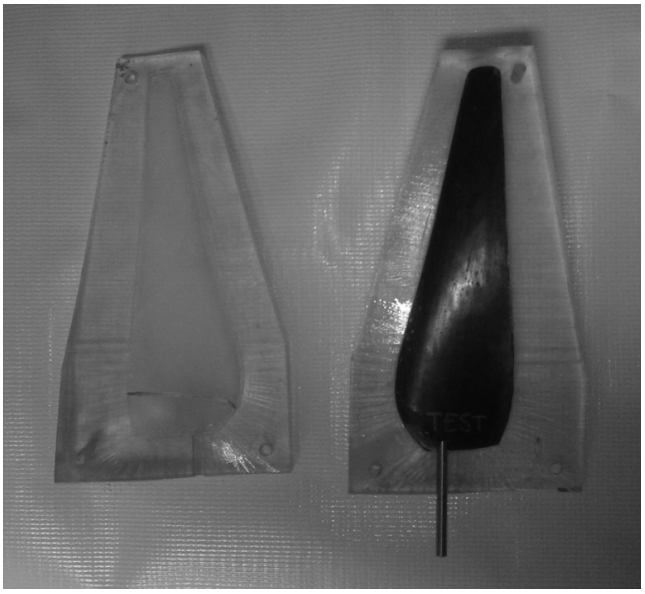

Fig. 18 Rapid prototyped molds with an example propeller blade.

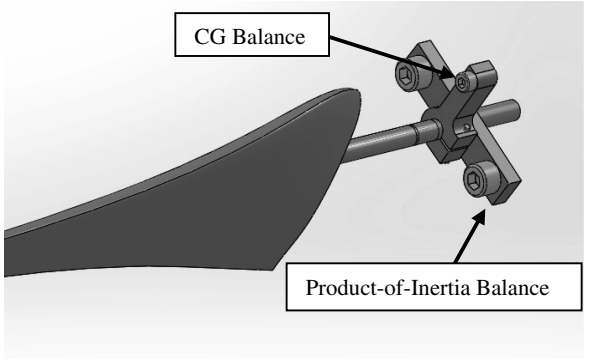

a)

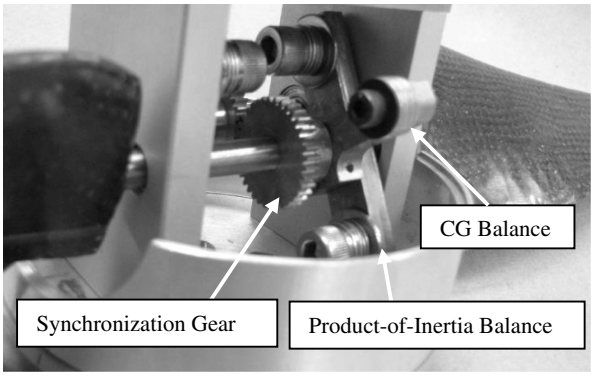

b)

Fig. 19 Mass balancing and synchronization gear installed on blade shaft: a) CAD model and b) as built.

with the principal axes directions:

$$\begin{bmatrix} I_{X'} \\ I_{Y'} \\ I_{Z'} \end{bmatrix} = \begin{bmatrix} (0.88, 0.47, 0.00) \\ (-0.46, 0.88, -0.11) \\ (-0.05, 0.10, 0.99) \end{bmatrix}$$

For the 8012, the inertia tensor was

$$I(X', Y', Z') = \begin{bmatrix} 10.47 & 0.00 & -0.53 \\ 0.00 & 10.47 & 0.97 \\ -0.53 & 0.97 & 0.87 \end{bmatrix} \text{oz} \cdot \text{in}^2$$

with the principal axes directions:

$$\begin{bmatrix} I_{X'} \\ I_{Y'} \\ I_{Z'} \end{bmatrix} = \begin{bmatrix} (0.88, 0.48, 0.00) \\ (-0.47, 0.87, -0.11) \\ (-0.05, 0.10, 0.99) \end{bmatrix}$$

Values for both the inertia tensor and principal axes matched well with an assumption of negligible mass imbalance effects.

The balanced blades were installed on the propeller hub with a small spur gear on each blade shaft (Fig. 19b) to synchronize the blades in the event of asymmetries. The entire assembly was then installed on a propeller test stand in the wind tunnel. The propeller test stand, shown in Fig. 20, was a custom two-component load balance designed for small propellers driven by electric motors, with a maximum capacity of 25 lb of thrust and 1 ft · lb of torque. Configuration and calibration of the load balance are described in [21].

Each test matrix was based on one of three base cases: a propeller speed of 3000, 4000, or 5000 RPMs at a velocity of 50 ft · s^{-1}. Once the base-case propeller speed was chosen, test points were set at tunnel velocities from 15 ft · s^{-1} to a maximum tunnel velocity at 5 ft · s^{-1} intervals, and propeller speed was determined by matching the Reynolds number of the base case, using the 75%R location for this Reynolds number matching. Each test consisted of two randomized replicates of the test matrix, with the test points that resulted in propeller overspeeding being dropped.

For each of the blade sets, 8009 and 8012, fixed-pitch tests were completed for comparison to the PVPP data by installing a friction lock on the propeller blade-pivot shafts. These tests were performed using 3000 RPM test matrices, and these data were used to compare the effectiveness of the PVPP configurations.

At the conclusion of fixed-pitch testing, the pitch lock was removed, and the propellers were tested in the PVPP configuration. Before each test, each blade was checked to make sure the blade pitch bearings remained free. Symmetry of the blade pitch and blade pitch limits were verified using indicator marks on the spinner plate. All data were corrected for wind-tunnel boundary effects using the Glauert correction [22].

Testing with the 3000 and 4000 RPM derived test matrices proceeded without incident. Several attempts at testing using the 5000 RPM test matrices resulted in significant vibrations and, on some occasions, slippage of the synchronizing gears or mass balances within the propeller hub. After these attempts, the 5000 RPM test matrices were removed from the test plan and all subsequent testing was performed using the 3000 and 4000 RPM test matrices.

Accumulated data for the two propellers at the two operating RPMs are shown in Figs. 21–25. The error bars for the PVPP data in these plots represent a 95% confidence interval of the mean, from samples collected over multiple tests, and multiple installations of the propellers in the tunnel, including cases when the propeller hub assembly was fully disassembled to replace the blade-shaft bearings.

Figure 21 shows the accumulated data runs of the 8012 propeller using 3000 RPM base test matrices. Also coplotted is the prediction from the PVQPROP code for the 8012 PVPP, assuming no limits to the blade pitch angle $\Delta\beta$. As predicted computationally, the 8012 propeller stayed at or near the blade angle for maximum efficiency over the range of advance ratios tested. At an advance ratio of

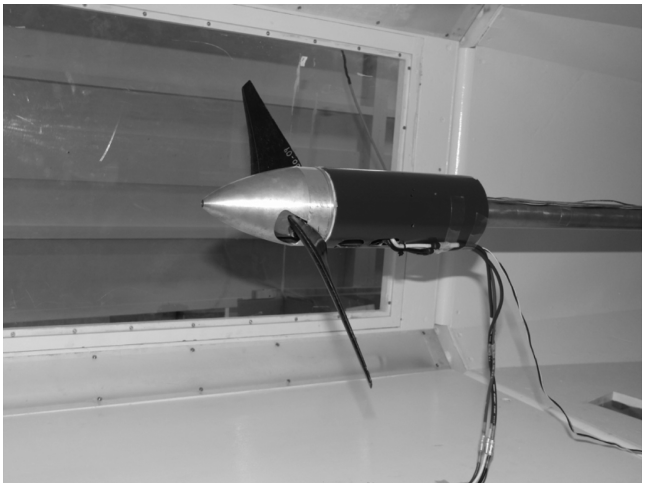

Fig. 20 8009 PVPP in the NCSU subsonic tunnel for testing.

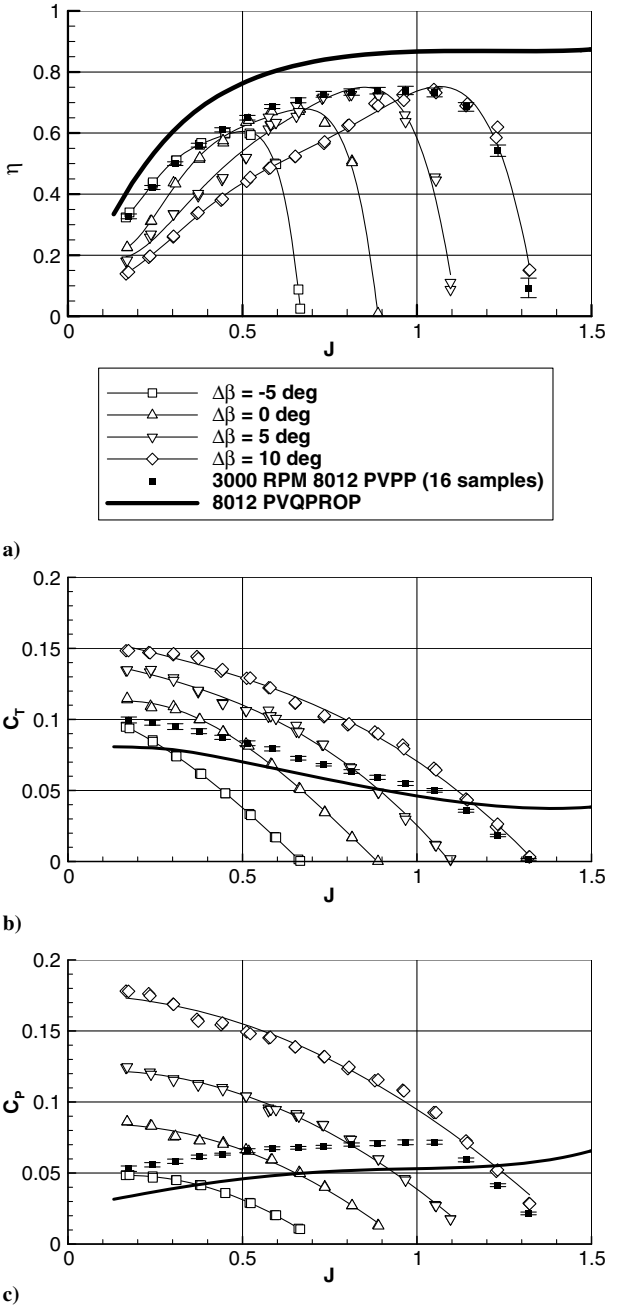

Fig. 21 Data for the 8012 propeller using a baseline propeller speed of 3000 RPMs and freestream speed of 50 ft · s^{-1}.

approximately 1.1, the blade reached the maximum-pitch-angle limit of travel imposed by a mechanical stop, and it subsequently tracked with fixed-pitch data. Blade pitch was evaluated by examining the intersection of fixed-pitch and PVPP data on C_P and C_T plots. At an advance ratio of 0.18, PVPP power and thrust data coincided with fixed-pitch data for a $\Delta\beta$ of -5 deg. As the advance ratio increased, the PVPP propeller reached $\Delta\beta$ angles of 0, 5, and 10 deg at advance ratios of 0.5, 0.85, and 1.1, respectively. Comparing these angles to those found using the PVQPROP code shows that predicted advance ratios are 0.4, 0.7, 0.95, and 1.25 for blade angles of -5, 0, 5, and 10 deg, respectively. This result indicates that the code underpredicted blade pitch angles. The magnitude of C_T and C_P data generally corroborates this observation, with experimental values of thrust and power coefficients being higher than predicted. This discrepancy between computational and experimental results could be attributed to several factors, including some structural flexing causing higher blade angles, a residual CG offset, or a dynamic imbalance. Further, although pitching behavior matched PVQPROP predictions well, the experimental propeller efficiency for both fixed and PVPP tests was significantly lower than computational predictions, indicating the airfoil performance parameters used in the inputs to the PVQPROP analysis were likely poorly approximated.

Similar trends can be seen in the 4000-RPM-based test matrix of the same propeller, shown in Fig. 22. The propeller adjusts to advance ratio changes but at slightly higher equilibrium pitch angles in comparison to the 3000 RPM results of Fig. 21 for any given advance ratio. At the lowest tested advance ratio of approximately 0.15, the PVPP propeller equilibrium pitch angle is approximately -2 deg. As the advance ratio increases, PVPP propeller data intersect with remaining fixed-pitch curves until reaching their maximum-pitch-angle mechanical stop at an advance ratio of approximately 1.05. Although the magnitudes of equilibrium pitch angles differed from computationally predicted

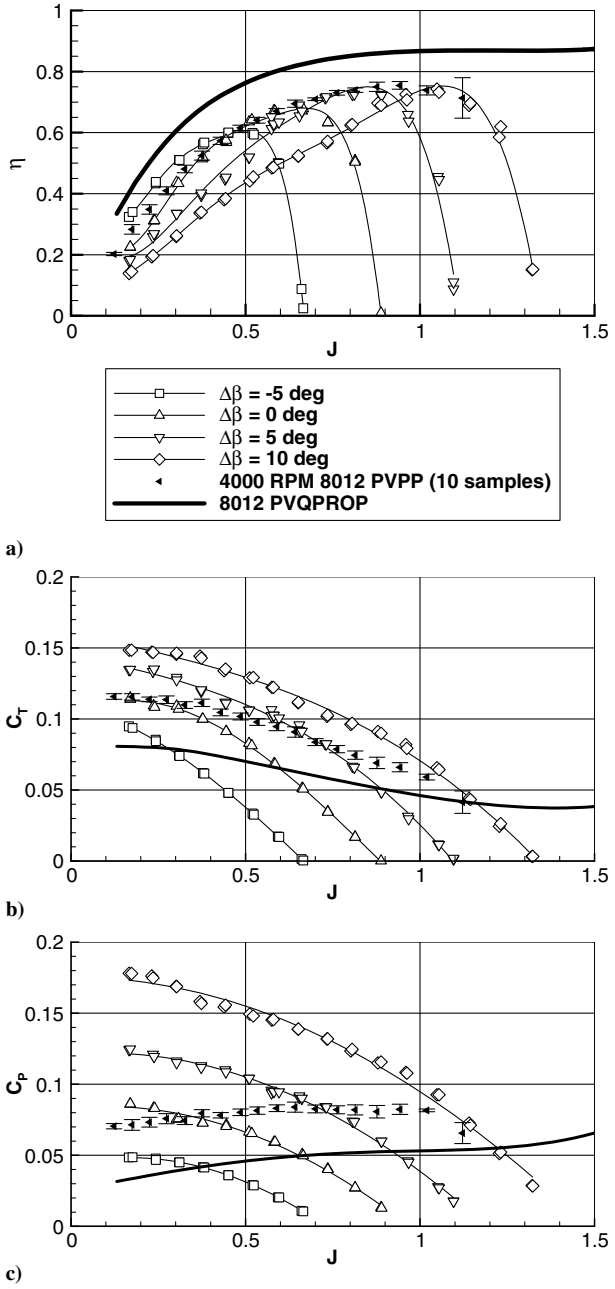

Fig. 22 Data for the 8012 propeller using a baseline propeller speed of 4000 RPMs and freestream speed of 50 ft · s^{-1}.

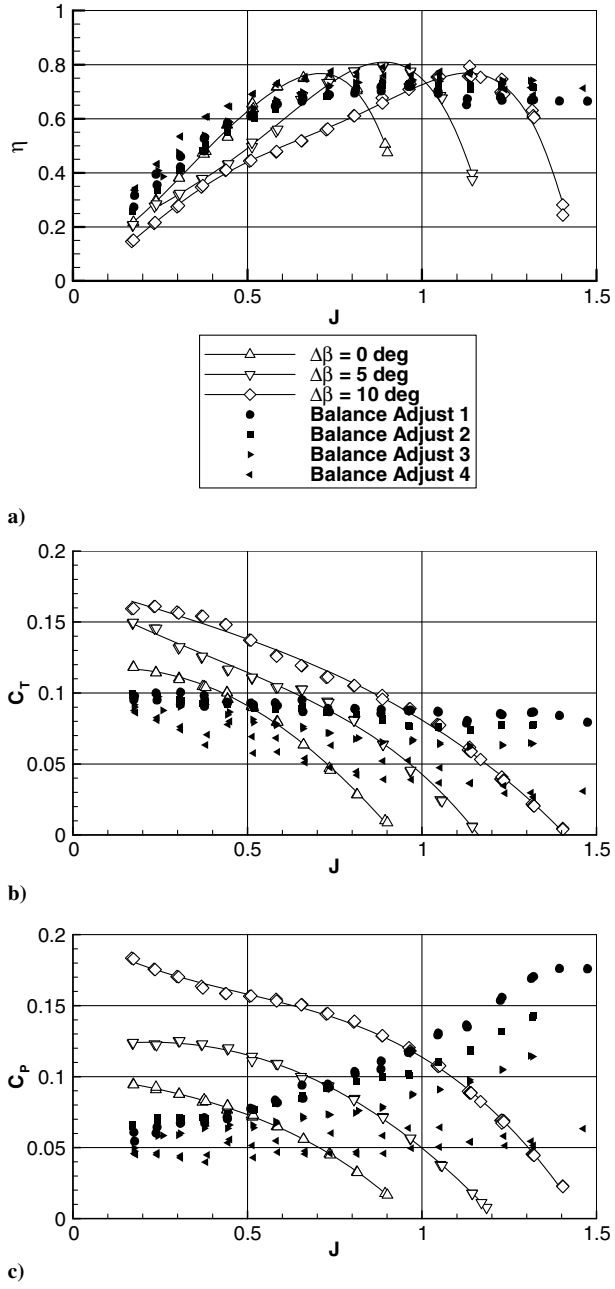

Fig. 23 Experimental data obtained while balancing blade products of inertia for the 8009 PVPP.

values, the overall behavior of the propeller matched very well with predictions.

Upon first testing the 8009 blades, the behavior of the blade pitch angle was much more aggressive than predicted. These results showed a significant increase in power coefficient with an increasing advance ratio, such that, as the advance ratio increased, the shaft power required to maintain RPMs rose dramatically. Operating under the assumption that this behavior was because of a difference in real and modeled inertial properties, the mass of the product-of-inertia balance was varied to compensate. When the mass in the product-of-inertia balance was increased, blade pitching took on the hysteresis behavior described in Sec. III.B and Fig. 10. Additional details of this behavior are provided in [21]. Reducing the mass of the product-of-inertia balance over a series of tests resulted in a flattening of the C_P curve to a profile similar to the computationally predicted behavior for a correctly mass-balanced PVPP. The change of the blade $I_{X'Y'}$ over the course of four test runs came to approximately 6.8×10^{-3} oz $\cdot$ in^2 per blade. The results for these four cases, shown in Fig. 23 along with the results for fixed-pitch cases, reinforce previous mass analysis findings, which showed that PVPP performance is sensitive to the value of the $I_{X'Y'}$ product-of-inertia term. With the final adjustment of the masses (shown as the dataset labeled "Balance Adjust 4") in Fig. 23, the results showed the expected and desired nearly constant power-coefficient variation with changing advance ratio.

Figures 24 and 25 show the accumulated data runs of the 8009 PVPP for the 3000 and 4000 RPM base test matrices, respectively. As seen with the results for the 8012 PVPP, the 8009 PVPP also stayed at or near the blade angle for maximum efficiency over the range of advance ratios tested. As with the 8012 propeller, the 8009 PVPP showed increased equilibrium pitch angles at higher RPMs. The increase in equilibrium angles seemed relatively consistent over the advance ratio range. Data from the 3000 RPM test matrices results in 0, 5, and 10 deg equilibrium pitch angles occurring at advance ratios

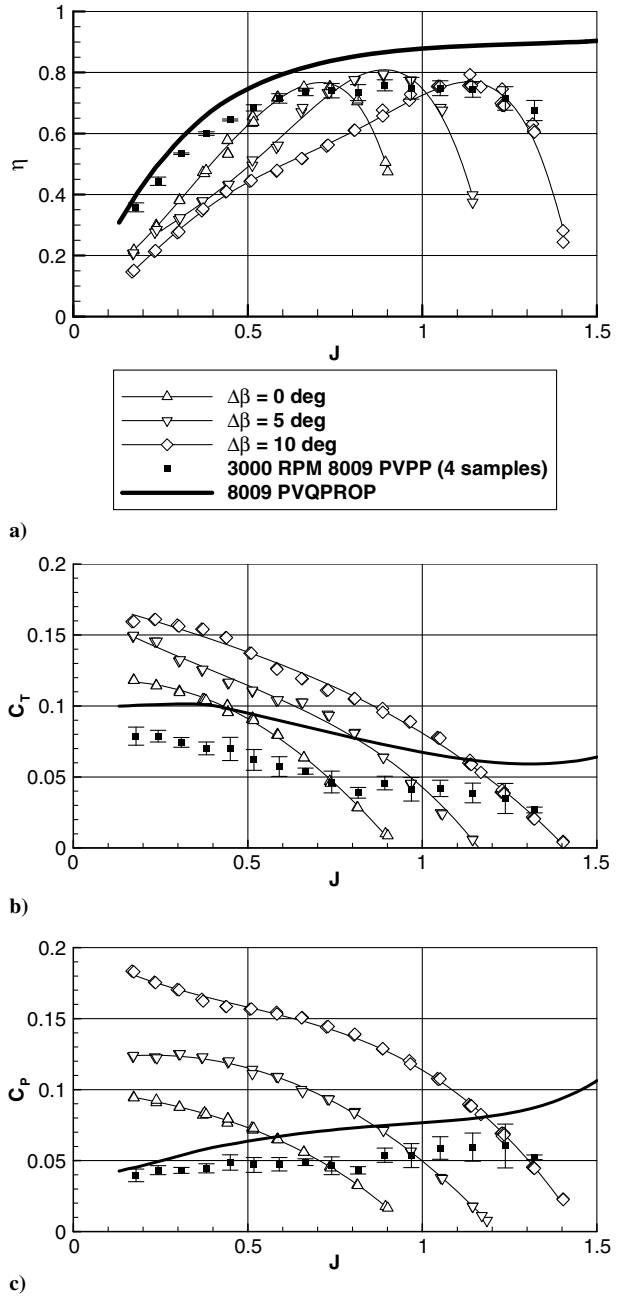

Fig. 24 Postadjustment data for the 8009 propeller using a baseline propeller speed of 3000 RPMs and freestream speed of 50 ft $\cdot$ s^{-1}.

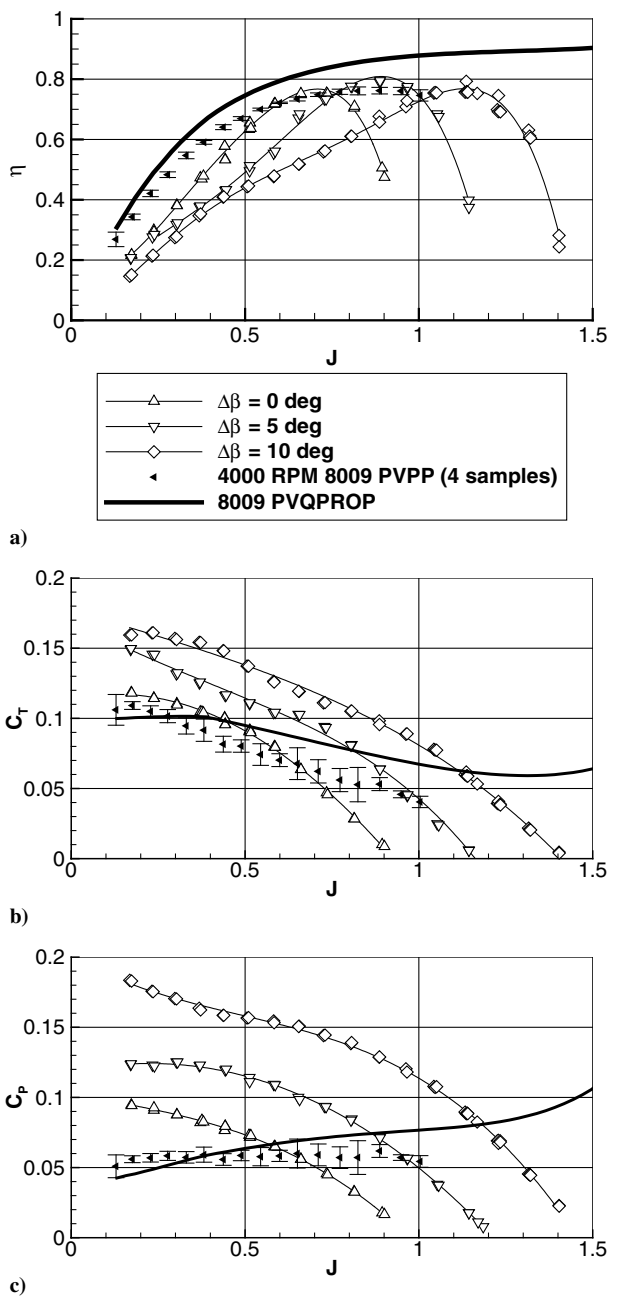

Fig. 25 Postadjustment data for the 8009 propeller using a baseline propeller speed of 4000 RPMs and freestream speed of 50 ft $\cdot$ s^{-1}.

Table 1 Technical specifications for the Converse aircraft: fixed pitch/PVPP

Parameter	Value
Span, in.	76.75
Chord, in.	11.75
Propeller	APC 18 × 8/8012 PVPP
Total weight, lb	19.10/19.72
Propeller plus spinner weight, oz	10.8/17.2
Motor	AXI 5345/14
Electronic speed control	Phoenix HV-110
Batteries	10S2P 10Ahr LiPo

of 0.75, 1.0, and 1.3, respectively. The higher 4000 RPM matrices shifted the 0 and 5 deg pitch angle equilibrium points to advance ratios of 0.65 and 0.95, respectively. Unlike the 8012 case, blade pitch angles for the 8009 PVPP were lower than PVQPROP-predicted values. Although higher pitch angles, due to the lower overall $x_{a.c.}$ values for the reduced static margin, were predicted analytically and computationally, the experimental results do not corroborate this behavior. Given the sensitivity of the initial 8009 blade performance to mass imbalances, it is likely that errors in measured or modeled inertial properties cause these discrepancies.

VI. Flight Demonstration

As a final proof of concept, a flight demonstration was conducted using the NCSU Flight Research Laboratory Converse unmanned aircraft. As shown in Fig. 26, the aircraft is a tractor configuration with an unswept constant-chord wing and conventional tail. It has tricycle landing gear and uses a standard off-the-shelf 72 MHz remote-control radio system for control. Table 1 lists the main specifications of the Converse aircraft and its electric motor-driven propeller.

To collect flight data, the aircraft was fitted with a simple flight data recorder (FDR) produced by Eagle Tree Systems, Inc.[‡] The FDR was instrumented to capture necessary motor/electronic speed controller performance data to evaluate propeller function during flight. The data channels, which were sampled at 10 Hz, included throttle command, motor RPMs, electronic speed control current and voltage, airspeed, and altitude. The flight computer and radio receiver were installed in the forward cargo bay; the batteries were mounted in the main overwing bay to minimize impact on the CG location.

Before flight operations, the aircraft control radio was programmed with an in-flight switchable throttle command limiter to ensure motor RPMs remained in the range tested in the tunnel. Flights were conducted on 6 May 2011, with the first flight using an off-the-shelf APC 18 × 8 Sport propeller. Total flight time for the APC 18 × 8 was 2 min and 45 s. After reviewing the first flight data, the test aircraft was switched from the fixed-pitch APC 18 × 8 to the 8012 PVPP. The throttle command limiter was engaged and, after a short taxi test, the second flight began. During the test, the aircraft was flown in circuits with ascents and descents in an attempt to introduce an advance ratio variation independent of motor RPMs. The throttle command limiter remained engaged during the entire PVPP flight. The aircraft was brought down after flying for 6 min and 20 s, and the FDR data were downloaded.

Although it is difficult to extract a meaningful estimate of thrust from the flight data, the FDR was configured to record battery-pack voltage and current draw, from which the electric power drawn can be calculated. To approximate a C_P calculation, the electrical power draw is used and 85% electrical efficiency is assumed for the electronic speed control/motor combination. These C_P data are plotted in Fig. 27 against the advance ratio calculated directly from flight data. It must be noted that the APC 18 × 8 and the 8012 PVPP have very different blade geometries. Even though the blade geometries are quite different, the results of these flight tests help show the significantly different performance of a PVPP compared to a typical fixed-pitch propeller. The APC 18 × 8 data in Fig. 27 show the typical fixed-pitch propeller dropoff in power coefficient as the advance ratio increases, whereas the PVPP propeller shows a power coefficient that remains steady in the 0.075–0.095 range, similar to the wind-tunnel testing results.

An alternate method to determine whether the PVPP propeller is behaving as designed is to examine whether there is a constant power draw at a given motor RPM, indicating a constant C_P. When the data from the two flights are plotted in this manner, much more significant scatter can be seen in the APC 18 × 8 data than in the 8012 PVPP data, as seen in Fig. 28. The C_P variation for the APC propeller, as with any fixed propeller, is heavily dependent on the advance ratio, such that power absorption at a specific RPM is dependent on freestream velocity. The PVPP propeller data show much tighter correlation between the propeller RPM and power draw, indicating that the C_P is relatively less dependent on the freestream velocity at any given RPM.

To mitigate some of the scatter from the variations in power draw during RPM transients, power can alternatively be plotted against throttle command. As seen from Fig. 29, these data show a similar, but tighter, correlation for the PVPP data than for the fixed-pitch APC 18 × 8 propeller data.

The results from the flight tests largely corroborate those obtained from the wind-tunnel tests and confirm that the PVPP successfully adjusts blade pitch angle over a range of advance ratios

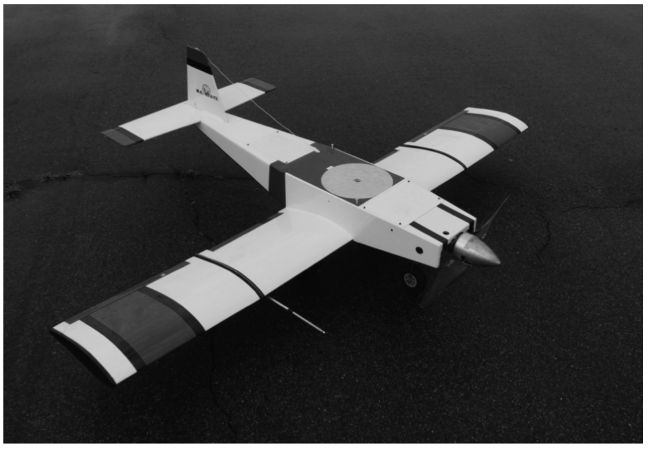

Fig. 26 NCSU Flight Research Converse unmanned vehicle.

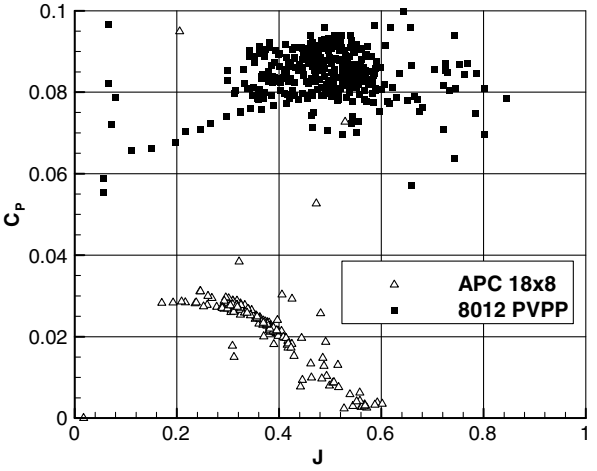

Fig. 27 Flight-test propeller C_P estimate: 1 point in 10 plotted.

[‡]Data available online at http://www.eagletreesystems.com [retrieved 20 July 2014].

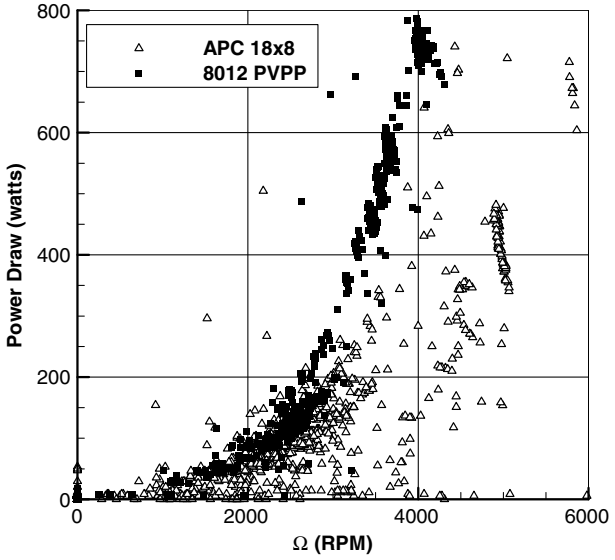

Fig. 28 Flight-test current draw variation over RPM envelope: 1 in 10 plotted.

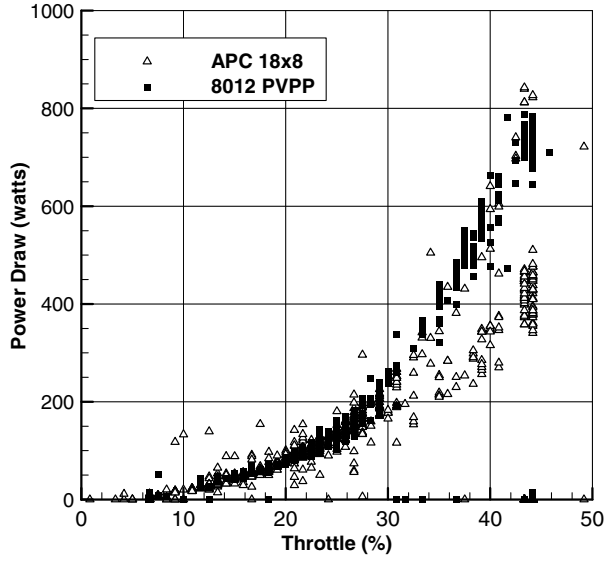

Fig. 29 Current draw over throttle command envelope: 1 in 10 plotted.

VII. Conclusions

The following conclusions are drawn from the analytical, computational, and experimental investigation of the PVPP concept:

1) A PVPP can be designed to use aerodynamic blade pitching moments on blades that are free to pitch about a radial pivot axis to achieve and maintain favorable pitch angles across a wide range of advance ratios. In comparison to the traditional fixed-pitch propellers that are often used on small manned and unmanned aircraft, the PVPP has a significantly wider high-efficiency operational envelope. Blades in a PVPP must be dynamically balanced so that inertial moments do not overpower aerodynamic moments.

2) It is possible to modify PVPP blade pitch behavior through tailoring of the blade geometric properties. Changes to the blade-pivot point and sweep result in changes to the blade static margin, as well as to the blade static margin variation with the advance ratio, respectively, which modifies the blade equilibrium pitch angle across the advance ratio.

3) The PVPP propeller can be designed such that the propeller absorbs constant power, at constant RPMs, over a wide flight envelope. This result allows a propeller to be matched to absorb full engine power from takeoff to high-speed dash, without the risk of engine overloading at low speeds. or engine overspeeding at high speeds.

4) Wind-tunnel and flight tests corroborate the wide performance envelope potential of the PVPP concept. Test PVPP articles demonstrated passive pitching over a range of 15 deg, limited only by mechanical stops. During the tests, the propellers maintained near-peak efficiency over the test range. Further testing must be performed to validate the sensitivity to blade sweep and static margin predicted computationally.

5) The PVPP concept realizes many of the well-known benefits of variable-pitch propellers while minimizing the weight and complexity associated with active propeller pitch control. Application of the concept can result in improved propulsion system performance, especially for small, light aircraft that operate over a wide range of flight speeds. Although the current work clearly demonstrates the benefits of the concept, further detailed flight experiments are needed to refine the concept, verify the sensitivity to geometry, and assess the degradation in performance due to mass imbalance or deviations in section pitching moments.

Acknowledgments

The lead author would like to thank the U.S. Air Force Research Laboratory for their sponsorship during much of computational effort presented in this work. We thank the reviewers and the Associate Editor for their insightful comments, which have resulted in improvements to the paper.

References

[1] Chanute, O., "Screws to Lift and Propel," *Progress in Flying Machines*, American Engineer and Railroad Journal, New York, 1894, pp. 58–59.

[2] Anderson, J. D., *Aircraft Performance and Design*, WCB/McGraw–Hill, Boston, 1999, pp. 156–162.

[3] Kinney, J., "Turning in the Wind: Frank W. Caldwell and the Variable-Pitch Propeller," *The ITEA Journal (The International Test and Evaluation Association)*, Vol. 30, No. 3, 2009, pp. 339–344.

[4] "Unmanned Aircraft Systems Roadmap 2005–2030," U.S. Dept. of Defense, Office of the Secretary of Defense, 2005.

[5] Miller, M., "MAV-2015 AFRL's Vision for Bird Sized UAV," *Proceedings of the 2011 International Technical Meeting*, The Inst. of Navigation, Manassas, VA, Jan. 2011, pp. 1–33.

[6] "Field Service Instructions for Aeromatic Propellers: Models 220, 220-I, and 220H," Koppers Company, Inc., Aeromatic Propeller Dept., Baltimore, MD, 1948, http://www.russellw.com/manuals/aeromatic_field_service/default.htm [retrieved 15 July 2014].

[7] Burger, C., and Hartfield, R., "Design, Testing and Optimization of a Constant Torque Propeller," AIAA Paper 2007-3927, 2007.

[8] Sandak, Y., and Rosen, A., "Aeroelastically Adaptive Propeller Using Blades' Root Flexibility," *Aeronautical Journal*, Vol. 108, No. 1086, Aug. 2004, pp. 411–418.

[9] Dwyer, W. J., and Rogers, J. B., "Aeroelastically Tailored Propellers," Soc. of Automotive Engineers TP-770455, Warrendale, PA, March 1977.

[10] Etkin, B., *Dynamics of Flight Stability and Control*, 3rd ed., Wiley, New York, 1996, pp. 25, 357–363.

[11] Kuethe, A., and Chow, C., *Foundations of Aerodynamics: Bases of Aerodynamic Design*, 5th ed., Wiley, New York, 1986, pp. 202–206.

[12] Drela, M., "QPROP Formulation," Massachusetts Inst. of Technology Aeronautics and Astronautics, Cambridge, MA, 2006, http://web.mit.edu/drela/Public/web/qprop/qprop_theory.pdf [cited 27 March 2015].

[13] Drela, M., "QPROP User Guide," Massachusetts Inst. of Technology Aeronautics and Astronautics, Cambridge, MA, 2007, http://web.mit.edu/drela/Public/web/qprop/qprop_doc.txt [cited 27 March 2015].

[14] Ol, M., Zeune, C., and Logan, M., "Analytical—Experimental Comparison for Small Electric Unmanned Air Vehicle Propellers," AIAA Paper 2008-7345, 2008.

[15] Drela, M., "XFOIL: An Analysis and Design System for Low Reynolds Number Airfoils," *Low Reynolds Number Aerodynamics*, edited by Mueler, T. J., Lecture Notes in Engineering, Vol. 54, Springer–Verlag, New York, 1989, pp. 1–12.

[16] Hibbeler, R., *Engineering Mechanics: Dynamics*, 11th ed., Pearson Prentice–Hall, Upper Saddle River, NJ, 2007, pp. 577–592, Chap. 21.

[17] Selig, M., *UIUC Airfoil Data Site* [online database], http://aerospace.illinois.edu/m-selig/ads/coord_database.html#E [retrieved 20 July 2014].

[18] Larrabee, E. E., "Practical Design of Minimum Induced Loss Propellers," Soc. of Automotive Engineers TP-790585, Warrendale, PA, 1979.

[19] Larrabee, E. E., and French, S. E., "Minimum Induced Loss Windmills and Propellers," *Journal of Wind Engineering and Industrial Aerodynamics*, Vol. 15, No. 1, 1983, pp. 317–327. doi:10.1016/0167-6105(83)90201-5

[20] Adkins, C. N., and Liebeck, R. H., "Design of Optimum Propellers," *Journal of Propulsion and Power*, Vol. 10, No. 5, 1994, pp. 676–682. doi:10.2514/3.23779

[21] Heinzen, S. B., "Development of a Passively Varying Pitch Propeller," Ph.D. Dissertation, North Carolina State Univ., Raleigh, NC, 2011.

[22] Barlow, J., Rae, W, and Pope, A, *Low-Speed Wind Tunnel Testing*, 3rd ed., Wiley, New York, 1999, pp. 433–435.